CHEMISTRY

Nanowire photochemical diodes for artificial photosynthesis

Virgil Andrei[1,2]†, Inwhan Roh[1,3]†, Peidong Yang[1,2,3,4,5]*

Artificial photosynthesis can provide a solution to our current energy needs by converting small molecules such as water or carbon dioxide into useful fuels. This can be accomplished using photochemical diodes, which interface two complementary light absorbers with suitable electrocatalysts. Nanowire semiconductors provide unique advantages in terms of light absorption and catalytic activity, yet great control is required to integrate them for overall fuel production. In this review, we journey across the progress in nanowire photoelectrochemistry (PEC) over the past two decades, revealing design principles to build these nanowire photochemical diodes. To this end, we discuss the latest progress in terms of nanowire photoelectrodes, focusing on the interplay between performance, photovoltage, electronic band structure, and catalysis. Emphasis is placed on the overall system integration and semiconductor-catalyst interface, which applies to inorganic, organic, or biologic catalysts. Last, we highlight further directions that may improve the scope of nanowire PEC systems.

INTRODUCTION

The sunlight received on Earth over 1 hour is sufficient to cover our total energy demands for 1 year (*1*, *2*). However, essential facilities, industrial processes, infrastructure, and combustion engines rely on fossil fuels, which provide a 20-times higher energy density in comparison with batteries (*2*–*4*). As a result, electricity still contributes less than 20% to our energy consumption (*1*). While a complete electrification of the economy is foreseeable in a distant future, the material resources and capital required to undertake major upgrades of legacy infrastructure pose immediate challenges to current economies. Hence, the sustainable production of carbon-neutral fuels from small building blocks such as water or atmospheric CO_2 is particularly desirable.

Photoelectrochemistry (PEC) provides one alternative toward renewable fuel production. In this case, photoexcited charges can be used to perform electrochemical processes, for example, proton reduction to hydrogen, or water oxidation to yield molecular oxygen. In this configuration, a photocathode is conventionally wired to a separate photoanode for unassisted fuel production, such as overall water splitting. A more elegant approach is presented through the photoelectrochemical diode, a concept that was introduced by Nozik in 1977 (*5*) and can be seen as a predecessor to the modern artificial leaf (*6*, *7*). In this case, a pair of semiconductors can be directly combined through an ohmic contact, resulting in a design coupling both oxidative and reductive half-reactions for overall fuel production. The resulting device structure mimics the operating principle of natural photosynthesis, in which two complementary light absorbers are necessary to couple carbohydrate synthesis to O_2 evolution. While this approach suits overall water splitting, CO_2 reduction (CO_2R) poses additional challenges including higher catalytic overpotentials or a control of the selectivity.

Semiconductor nanowires present a number of advantages that are key to overcoming those challenges (*8*). First, nanowires have a high surface area that can accommodate more active sites or allow higher catalyst loadings, translating to an increased turnover of the light-driven reaction. Second, photoelectrochemical nanowires are known to enhance charge separation, as photoexcited carriers only need to travel a short distance to the semiconductor-electrolyte interface. This is crucial for preventing charge recombination in materials with short carrier diffusion lengths, such as transition metal oxides (*9*). In contrast to a flat semiconductor, nanowire arrays further suppress reflection, which, in turn, improves light absorption. This light-trapping effect occurs because of the orientation of the nanowires and their variable refractive index, which enhance light scattering within the array. Last, nanowire arrays provide a considerable control over the mass transport inside the array, which can be accordingly simulated and adjusted for an increased reactivity (*8*). In this review, we take a closer look at how these factors govern the performance of nanowire photoelectrodes for solar fuel production. Furthermore, we evaluate the role of the catalyst interface for a wider product scope and extract general design principles toward system integration.

DESIGN PRINCIPLES FOR NANOWIRE PHOTOCHEMICAL DIODES

Because of their unique properties, nanowires provide a multitude of handles to steer the efficiency and selectivity of photoelectrocatalysis. For example, the fabrication of nanowire arrays can affect their light absorption through the choice of diameter, length, and spacing, whereas the presence of heterojunctions, passivating layers, or surface-bound catalysts can alleviate the photovoltage requirements for a given half-reaction. These considerations become particularly relevant in case of unassisted devices combining two light absorbers for overall solar fuel production, where factors including photocurrent or bandgap matching need to be further considered. To provide a complete picture of the opportunities available in nanowire PEC, we take a closer look at these design principles below.

[1]Department of Chemistry, University of California, Berkeley, Berkeley, CA 94720, USA. [2]Materials Sciences Division, Lawrence Berkeley National Laboratory, Berkeley, CA 94720, USA. [3]Liquid Sunlight Alliance, Lawrence Berkeley National Laboratory, Berkeley, CA 94720, USA. [4]Department of Materials Science and Engineering, University of California, Berkeley, Berkeley, CA 94720, USA. [5]Kavli Energy NanoScience Institute, Berkeley, CA 94720, USA.
*Corresponding author. Email: p_yang@berkeley.edu
†These authors contributed equally to this work.

History

To understand the design principles behind nanowire PEC, we first need to look back at its development throughout the years. Semiconductor nanowires have been synthesized since the 1990s through a range of techniques including vapor-liquid-solid (VLS) growth (*10*, *11*), etching (*12*, *13*), or laser ablation (*14*). While VLS and etching methods remained very popular, an entire range of template-directed methods have been developed in the meantime (*15*). Originally, a vast amount of literature only reported fundamental studies of their material and physicochemical properties (*16*, *17*). These properties are conventionally probed by means of scanning electron microscopy (SEM), transmission electron microscopy, energy-dispersive x-ray spectroscopy, x-ray diffraction analysis, or surface area techniques, whereas two- and four-point probe stations are necessary to determine the electronic and thermal properties of individual nanowires (*15*).

Nanowire arrays first found application as photoelectrodes in dye-sensitized solar cells (*18*–*23*). In this case, a ruthenium-based dye was coating ZnO nanowires, which replaced the conventional micrometer-thick films of oxide nanoparticles. This proved beneficial in collecting photoexcited carriers by avoiding the trap-limited diffusion process, which accounts for electron transport in nanoparticle films (*19*). Nanowire-based (photo)electrodes later expanded to a wide range of energy applications beyond photovoltaics (*24*), including pollutant degradation (*25*, *26*), batteries (*27*, *28*), and supercapacitors (*28*–*30*).

Similar nanowires were also used for photoelectrochemical fuel production in a range of configurations. Individual photoelectrodes could either be synthesized in the shape of randomly oriented nanowires on a conductive substrate (*31*) or as oriented nanowire arrays with a controlled growth (*32*, *33*), depending on the deposition technique and desired properties (Fig. 1, A and B). Some of the earliest reports of overall water splitting involved both nanowire arrangements. For example, bilayer nanowire meshes could be assembled from Ru/Rh-$SrTiO_3$ and $BiVO_4$ nanowires (*34*), whereas TiO_2 nanowires were grown onto larger Si nanowires in a so-called nanotree heterostructure (*35*). These systems took the original concept of a photochemical diode and expanded it toward a nanowire structure, as illustrated in Fig. 1C (*36*, *37*). As opposed to Nozik′s prototypes (*5*), where an opaque ohmic contact (metal layers bonded by a silver epoxy cement) meant that both semiconductors need to be irradiated separately, these nanowire designs enabled a single optical path, which corresponds to the natural sunlight irradiation. This concept of nanowire-based photochemical diodes was initially proposed in the Department of Energy Helios Program at Lawrence Berkeley National Laboratory in the early 2000s (*38*, *39*) and was later propagated into the Energy Hub Joint Center of Artificial Photosynthesis.

PEC performance

While nanowire photoelectrodes can be synthesized in a wide range of shapes and configurations, further factors need to be taken into account when designing a high-performance photoelectrochemical diode. In general, the solar-to-fuel (STF) conversion efficiency of a photoelectrochemical device depends on the photocurrent or product amount obtained under operation. In case of an unassisted tandem PEC device, the bias-free photocurrent and operating voltage correspond to the point where the individual photocurrent traces of the photocathode and photoanode intersect (Fig. 1D) (*40*). Ideally, both electrodes display high photocurrents, providing a large overlap between the photocathode and photoanode traces, which translates to a high bias-free photocurrent and early onset bias voltage of the corresponding two-electrode PEC device (Fig. 1E). In a real case, photoelectrode onset potentials may be delayed because of high catalyst overpotentials, while photocurrent mismatch between the two electrodes may further decrease the photocurrent overlap. In turn, these effects can shift the operating voltage (V_{op}), which determines the potential applied onto an electrocatalyst under bias-free operation.

Other important aspects to keep in mind are the bandgap, absorption, and transmittance of the top light absorber, which determine how much light reaches the bottom light harvester in a tandem PEC configuration. Two semiconductors of similar bandgaps will yield a low overall photocurrent, as the top light absorber filters most of the usable solar spectrum, which substantially diminishes the photocurrent of the bottom absorber (*41*). Accordingly, most PEC and photovoltaic (PV) models predict maximum tandem efficiencies for top and bottom semiconductors with bandgaps of 1.6 to 1.7 and 0.95 to 1.0 eV, respectively, depending on solar spectrum, light concentration, and catalyst activity (*42*, *43*). These theoretical efficiencies can amount to 20 to 30% for solar-to-hydrogen (STH) conversion (*43*). The optimal configuration becomes more challenging to evaluate for nanowire diodes, as light can be either transmitted directly or filtered through the top light absorber depending on the nanowire density and morphology. A nanostructured electrode may also introduce substantial light scattering.

Stability is also an important factor for these devices to be environmentally and economically practical. The high surface area of the nanowire geometry and the synthetic conditions to produce nanowires generally lead to the presence of surface defects. Surface defects can lead to the pinning of the Fermi level (*44*), which reduces PEC device efficiency and induces photocorrosion, resulting in the degradation of the photoelectrodes (*45*). In general, photoelectrodes need to be protected using passivating and charge carrier selective layers (*46*, *47*), whereas high–surface area materials require additional consideration to prevent any site from being exposed to the environment. Demonstrations of stability using diurnal cycling to simulate real conditions are also necessary to show the behavior of the device when returning to open circuit conditions for extended periods of time (*48*). The potential switching resulting from illumination to dark can induce failure due to corrosion or contamination, as observed in case of planar systems. For example, the lack of SiO_x formed under illumination leads to a rapid corrosion of Si under the dark (*49*), while carbonaceous impurities (*48*) and catalyst dissolution (*50*) can affect the activity of Pt.

Nanowire semiconductor design

Bandgap

Careful design of the light absorber is a first step to improving the overall performance of PEC devices. While one-dimensional nanowires offer several benefits as described earlier, band behavior and nanowire geometry must also be considered. Photoabsorbers require suitable band positions to drive reactions such as water oxidation, proton reduction, or CO_2R. For example, the half-reactions

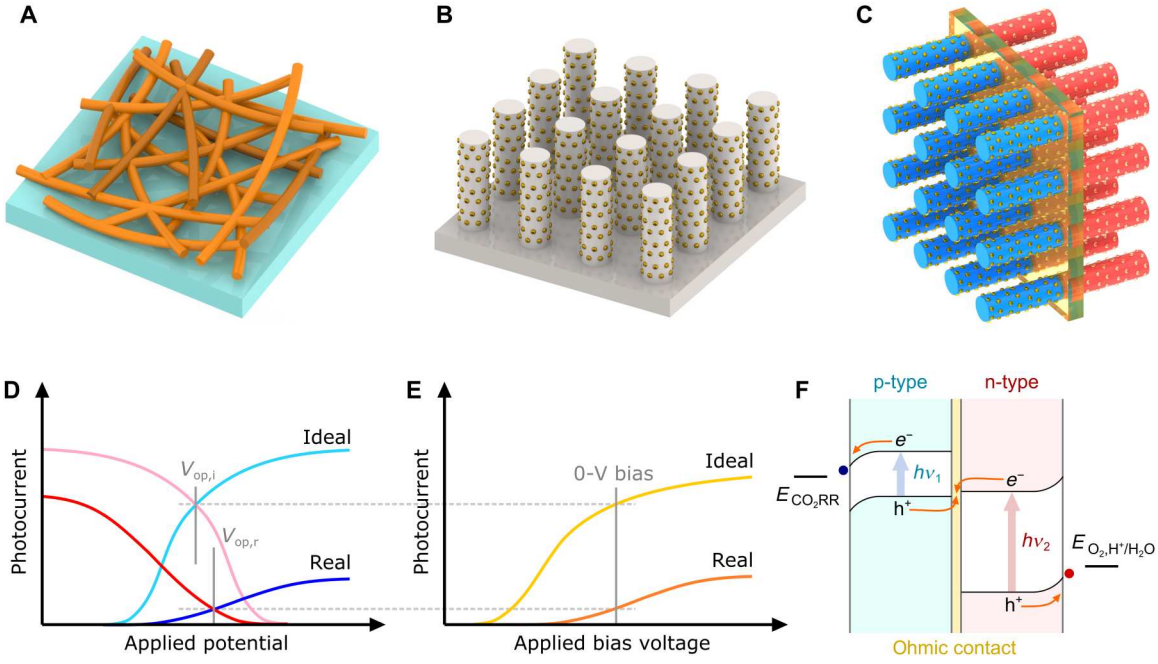

Fig. 1. Conventional PEC nanowire structures. (**A**) Randomly oriented nanowires on a conductive substrate (e.g., FTO|Fe_2O_3) (*31*). (**B**) Ordered nanowires, which are grown or etched into a solid wafer (as in the case of Si). (**C**) Concept of a nanowire photochemical diode, where two nanowire arrays are interfaced through a transparent ohmic contact. (**D**) Overlap of the photocathode (red) and photoanode (blue) traces for a real device and in an ideal case. (**E**) Photocurrent traces of the corresponding bias-free PEC tandem devices. In this example, the overall device photocurrent is limited by the lower photocurrent of the photoanode (*40*). (**F**) Schematic energy diagram of a photochemical diode coupling a CO_2R reaction (CO_2RR) with water oxidation, as depicted in (C).

for water splitting are

$$2H^+ + 2e^- \rightarrow H_2 \; E^0_{H^+/H_2} = 0 \text{ V versus RHE} \quad (1)$$

$$2H_2O \rightarrow O_2 + 4H^+ + 4e^- \; E^0_{O_2,H^+/H_2O} = 1.23 \text{ V versus RHE} \quad (2)$$

and select half-reactions for CO_2R are

$$CO_2 + 2H^+ + 2e^- \rightarrow CO + H_2O \; E^0_{CO_2/CO} = -0.11 \text{ V versus RHE} \quad (3)$$

$$2CO_2 + 12H^+ + 12e^- \rightarrow C_2H_4 + 4H_2O \; E^0_{CO_2/C_2H_4} = 0.08 \text{ V versus RHE} \quad (4)$$

where the potentials are given against the reversible hydrogen electrode (RHE).

The photocurrent can be improved by selecting semiconductors with suitable bandgaps, which can use a wider range of the visible spectrum. A wider bandgap can also increase the photovoltage, resulting in an earlier onset potential for the reaction of interest (*51*). For bias-free PEC devices, the total photovoltage supplied by the system needs to be larger than the thermodynamic requirement of the two half-reactions. This means that the semiconductors must supply at least 1.23 V for water splitting or 1.34 V for CO_2R to CO coupled with water oxidation. However, reaction kinetics, surface interactions, or local concentration gradients lead to additional overpotentials in real-world systems, which usually contribute a few hundred millivolts to the minimum required voltage.

Band bending and depletion region

Band bending and the width of the depletion region further influence charge extraction and the nanowire photovoltage. Band bending occurs when a semiconductor interfaces with the electrolyte and the Fermi levels equilibrate (Fig. 2A). This bending creates a depletion region in which the formed electric field drives mobile charge carriers away and influences the photovoltage, which arises from the splitting of quasi-Fermi levels that are generated by illumination (*52*). However, for thin nanowires, the diameter of the nanowire may be smaller than the width of the depletion region (Fig. 2B). This effect can be seen in the recombination rates, which, for a thin n-type nanowire, are given by Eqs. 5 and 6

$$J_{\text{bulk r}} = \frac{qD_p n_i^2 (D - 2w)}{8N_D L_P^2} \left(e^{\frac{qV}{k_B T}} - 1\right) \quad (5)$$

$$J_{\text{depl r}} = J_{\text{depl r,planar}} + \frac{qn_i Z(D, w) D_p}{2r_{\text{depl r,max}} L_P^2} e^{\frac{qV}{2k_B T}} \quad (6)$$

$J_{\text{bulk r}}$ and $J_{\text{depl r}}$ refer to the recombination rates in the bulk and in the depletion region for a nanowire, respectively. k_B is the Boltzmann constant. T is the temperature. q is the elementary charge. D_p is the hole diffusion constant. n_i is the intrinsic carrier concentration. N_D is the dopant concentration. L_P is the hole diffusion length. $r_{\text{depl r,max}}$ is the radial position of maximum recombination rate in the depletion region, and $Z(D, w)$ is the effective recombination area as defined by explicit integral over D and w. A more in-depth

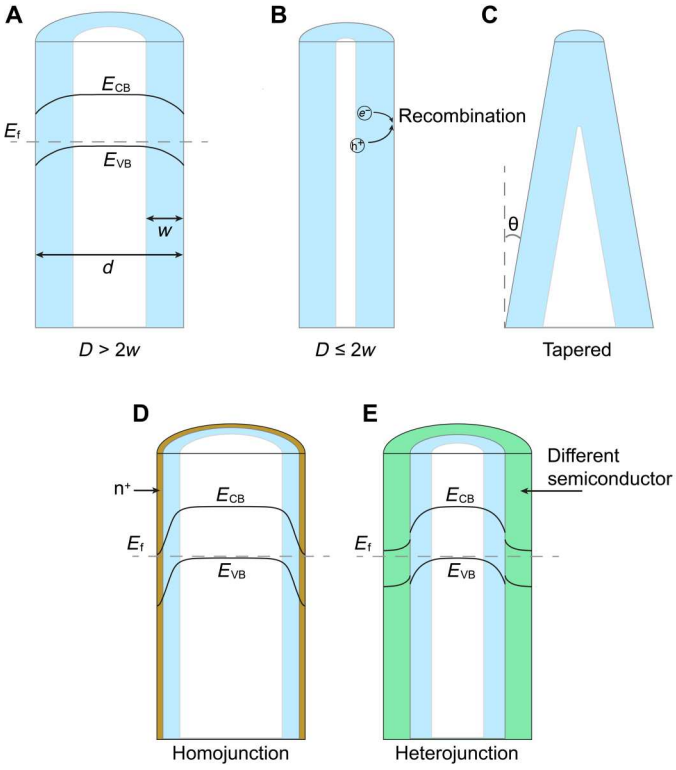

Fig. 2. Band bending in nanowire designs. (**A**) Nanowire with a diameter (*D*) larger than the depletion region width (*w*). (**B**) Nanowire with a diameter smaller than depletion region width. (**C**) Tapered nanowire. (**D**) Radial homojunction in the nanowire. (**E**) Radial heterojunction on the nanowire.

analysis and derivation of these equations are found in an earlier report (*53*). For a thin nanowire, the second term in Eq. 6 becomes notable, leading to large recombination rates and a weak interfacial electric field. This weak electric field causes a weak drift current, which means improper charge separation, resulting in decreased photovoltages and photocurrents (*54*). This also becomes problematic in tapered nanowires (Fig. 2C), where portions of the nanowire are too narrow to properly separate and extract charges, leading to the same effects as described above (*53*).

One possible strategy to reduce the width of the depletion region while simultaneously increasing the photovoltage is by introducing a buried junction (Fig. 2D). Radial junctions can be easily made on nanowires because of their one-dimensional geometry. Introducing a radial junction by doping p-type silicon nanowires with an n^+ layer has been shown to increase the photovoltage up to 300 mV by making the band bending dependent on the n^+p junction rather than the interface with the electrolyte, thus allowing the photovoltage to be maintained across electrolytes of varying pH from 3 to 9 (*55*) while also showing no degradation after 24 hours (*46*). This was also shown for gallium phosphide nanowires where the diameter of the nanowire was less than that of the depletion region and resulted in poor performance. When doping the surface with zinc, the width of the depletion region decreased substantially, allowing for higher photovoltages and photocurrents (*56*). Proper management of nanowire diameters, band bending, and depletion regions allow for more efficient charge separation, which translates to higher photovoltage, photocurrent, and stability. However, excessive concentrations of dopants can lead to increased rates of recombination, so care is needed in forming these buried junctions.

Passivation layers

Photocurrent and stability can also be improved by adding one or more layers onto the nanowire photoelectrodes (Fig. 2E). Inert transparent layers are typically grown on top of the semiconductors to prevent electrolyte exposure, passivate surface states, and promote charge separation by acting as an electron- or hole-selective layer (*57*, *58*). The most commonly used layer, TiO_2, can stabilize Si, GaAs, and GaP for oxygen evolution over 100 hours in 1 M KOH (*47*). Ideally, the charge carrier should be transported across these layers ballistically to maximize efficiency, but additional layers onto the surface may introduce other effects such as reduced conductivity, band level pinning, and unwanted catalytic behavior (*59*–*61*). For example, TiO_2 can get reduced under cathodic conditions, which either leads to oxygen vacancies that trap electrons (*61*) or the presence of metallic Ti, which behaves as a hydrogen evolution catalyst (*62*).

It has also been shown that band pinning could occur when these layers interface with the electrolyte. When using Pt nanoparticles on TiO_2-passivated Si (i.e., the electrolyte was in contact with both Pt and TiO_2), the conduction band was pinned to −0.23 V versus RHE, creating a barrier for the electrons from reducing Fe(III) until the applied potential was 0.75 V versus RHE. If TiO_2 was not used or a Pt film was used instead (so the electrolyte does not contact TiO_2), then the photoelectrode was capable of reducing Fe(III) at 1.28 V versus RHE, which is the expected potential based off the semiconductor photovoltage (*46*). As a result, the desired reaction may not happen at the expected potential because of the interaction of additional layers on the surface.

Nanowire geometry

Choosing the appropriate nanowire geometry also plays an important role in increasing the efficiency of a PEC device. As mentioned earlier, nanowires with diameters thinner than the width of the depletion layer suffer from poor charge separation. In addition, nanowire geometry has been shown to affect the wavelength of light absorbed. For the same height, silicon nanowires exhibit larger overall optical absorption than their planar counterparts (*63*), whereas ordered arrays absorb more photons than nonordered samples (*64*). However, the wavelength of absorbed light is dependent on the diameter, pitch, and length of the nanowires (*65*). For a nanowire array with a diameter of 50 nm, a pitch of 100 nm, and a length of 1000 to 4000 nm, absorption was near 1 for wavelengths above 440 nm but dropped to 0 for wavelengths below 620 nm (*63*). This could be shifted to longer wavelengths by increasing the pitch up to 700 nm (*66*). In general, absorption increases at diameters and pitches of similar length to the incoming light (*65*). The angle of light incidence also affects light absorption. For example, the largest short-circuit current in silicon nanowires was seen when physically rotating the array by 35° (*67*), whereas the optimal inclined angle of GaN nanowires was calculated to be 0.6° (*68*).

The nanowire geometry also controls the surface area, which can influence the photocurrent and product selectivity. In the case of nanowire photoelectrodes, the optimal surface area for a nanowire photoelectrode must balance the photovoltage loss from increased surface area and catalytic enhancement from increased catalyst loading. The activity of a catalyst toward a reaction can be described

by the Tafel equation

$$\eta = a + b \log J \tag{7}$$

where η is the overpotential, a is the intercept given by the exchange current density, b is the Tafel slope, and J is the current density. The Tafel slope, conventionally reported with units of millivolts per decade, describes how much overpotential is needed to increase the current 10-fold in an ideal system. These values can be compared with the photovoltage loss coming from a textured semiconductor through

$$V_{ph}(J) = \frac{2.3nk_BT}{q}\log\left(\frac{|J_{sc}| - |J|}{R|J_0|} + 1\right) \tag{8}$$

where V_{ph} is the photovoltage, n is the diode quality factor, J_{sc} is the short-circuit current, R is the roughness factor, and J_0 is the dark current density or recombination current. To see improvements in performance, the reduction in photovoltage must be smaller than the reduction in overpotential for the specified reaction, or, in other words, reactions with sluggish kinetics are more likely to see improvements due to increased surface despite the lower photovoltage. However, variations in J_0 and n due to fabrication can lead to a disparity between experimentally observed losses of photovoltage and predicted values (*69*).

Catalysis

Besides increasing the photovoltage, a similar effect on the PEC device performance can be obtained by using selective catalysts with low overpotentials and high turnovers toward a desired reaction. Tailored catalysts can efficiently use photogenerated carriers to perform water oxidation, proton reduction, or CO_2R, alleviating overpotentials occurring at the semiconductor-electrolyte interface. Table 1 shows several examples of electrocatalysts that demonstrate

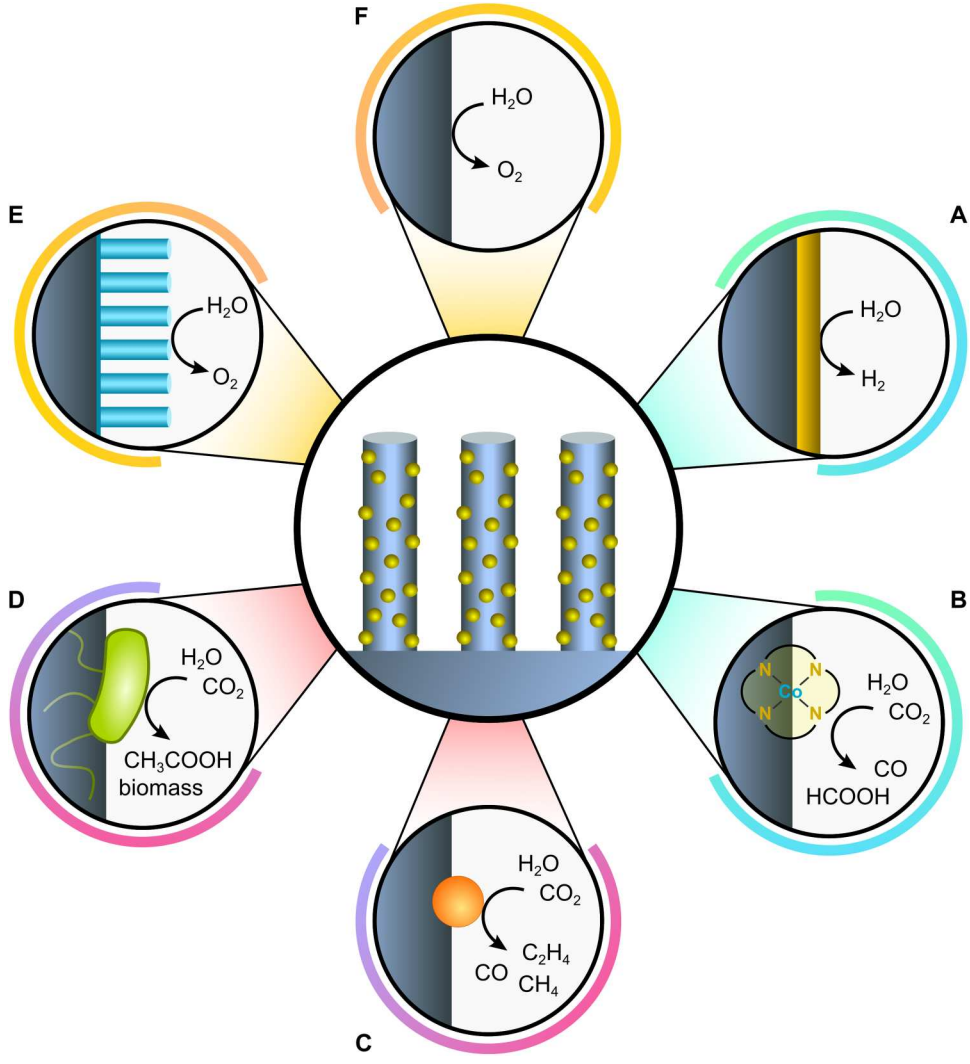

Fig. 3. Design principles for nanowire photoelectrodes. Nanowires can be used for proton and CO_2R to small products (blue halo) (**A** and **B**), higher value multicarbon synthesis (red) (**C** and **D**), or water oxidation (yellow) (**E** and **F**). Light harvesting nanowires can form a direct semiconductor-electrolyte interface (F), or they can be coated with suitable electrocatalytic, passivating, or charge-selective nanostructures. These nanostructures include conformal coatings (A), nanoparticles (C), flakes, or nanowires (E). Specific inorganic (C), molecular (B), or biocatalysts (D) are often required to attain high selectivity toward carbon-based products. These catalysts can be interfaced to the nanowire surface through direct deposition (C), anchoring groups (B), or flagella/pili growth (D) (*117*).

Table 1. Comparison between the performance of electrocatalysts for oxygen evolution and CO_2R. These catalysts requiring low overpotentials may be suitable for PEC systems. J_{prod}, partial current density; FE, faradaic efficiency toward the desired product.

Catalyst	Performance at J_{prod} = 0.5 mA cm^{-2}		Performance at J_{prod} = 1.0 mA cm^{-2}		Electrolyte	Stability (hours)	Reference
	E (V versus RHE)	FE (%)	*E* (V versus RHE)	FE (%)			
Oxygen evolution (O_2)							
Fe-Mn-O nanosheet	1.42		1.44		1 M KOH	2500 cycles	(*192*)
Single Co on TiO_2	1.52		1.54		1 M KOH	42	(*193*)
$MoS_2/Co_9S_8/Ni_3S_2$/Ni	1.27		1.28		1 M KOH	24	(*194*)
Mn-doped RuO_2	1.32		1.34		1 M H_2SO_4	5.6	(*195*)
Amorphous IrO_x	1.41		1.42		1 M H_2SO_4	24	(*196*)
CO_2 → CO							
Oxide-derived Au	−0.27	77	−0.29	83	0.5 M $NaHCO_3$	8	(*197*)
Single Fe^{3+} on N-doped carbon	−0.27	83	−0.29	85	0.5 M $KHCO_3$	12	(*198*)
Au nanoneedles	−0.23	69	−0.24	75	0.5 M $KHCO_3$	8	(*199*)
Au-NOLI	−0.37	74	−0.41	93	0.1 M $KHCO_3$	8	(*200*)
CO_2 → $HCOO^-$							
B-doped Bi	−0.4	54	−0.44	67	0.1 M $KHCO_3$	13	(*201*)
Partially oxidized Co atomic layers	−0.18	22	−0.19	30	0.1 M Na_2SO_4	12	(*198*)
Single-atom Pb on Cu	−0.32	78	−0.43	89	0.5 M $KHCO_3$	–	(*202*)
CO_2 → CH_3OH							
5 nm CoNP on N-doped graphene	−0.1	35	−0.15	53	0.1 M $NaHCO_3$	10	(*203*)
Pd/SnO_2 nanosheet	−0.18	45	–		0.1 M $NaHCO_3$	25	(*204*)
CO_2 → C_2H_5OH							
Dense Cu nanowires	−0.58	9	−0.62	13	0.1 M $KHCO_3$	1	(*205*)
Amorphous CuTi alloy	−0.50	9	−0.60	12	0.1 M $KHCO_3$	3 months	(*206*)
CoO on N-doped carbon	−0.32	55	−0.37	61	0.5 M $KHCO_3$	5.5	(*207*)
CO_2 → C_2H_4							
CuO nanoplates	−0.45	16	−0.50	25	0.5 M KCl	24	(*208*)
O_2 plasma Cu	−0.63	13	−0.67	12	0.1 M $KHCO_3$	5	(*209*)
Cu nanoparticle ensemble	−0.66	11	−0.69	16	0.1 M $CsHCO_3$	10	(*210*)

low overpotentials at moderate current densities, making them potential candidates for use in a PEC device.

By taking into account the reaction overpotentials of state-of-the-art catalysts, one can quickly assess which components are needed in a bias-free PEC device. The full cell voltage required to drive a reaction at a partial current density of 0.5 or 1.0 mA cm^{-2} can be calculated using Table 1 by subtracting the potentials of the corresponding anodic and cathodic half-reactions. For example, platinum and amorphous iridium oxide catalysts operate at applied potentials of −0.02 V versus RHE for H_2 evolution and 1.42 V versus RHE for O_2 evolution, respectively, amounting to a 1.44 V photovoltage for overall water splitting. Similarly, coupling CO_2R with O_2 evolution demands 1.71 V using oxide-derived Au for CO_2-to-CO conversion or 2.11 V with Cu nanoparticle ensembles for CO_2-to-C_2H_4 reduction.

The activity of a given electrocatalyst can also depend on the local environment, morphology, and its interface with the underlying catalyst support. Semiconductor substrates could lead to increased overpotentials and differing selectivities over catalysts deposited on dark electrodes. For example, in the previous simplified analysis, we would expect TiO_2 to drive overall water splitting given that its photovoltage of ~1.6 V is more than the calculated value of 1.44 V. However, in Fujishima and Honda's (*70*) pioneering demonstration of unassisted O_2 evolution, the corresponding cathodic reaction was Fe^{3+} reduction rather than H_2 evolution to ease voltage requirements, suggesting that TiO_2 cannot perform overall water splitting in itself. Indeed, illuminated TiO_2 coupled with O_2 evolution catalysts shows onset potentials above 0.1 V versus RHE (Table 2) instead of an expected onset of around −0.2 V versus RHE, suggesting that ~300 mV of photovoltage is lost. A possible reason for this discrepancy is the level of the conduction band, ~2 eV below the redox potential for oxygen evolution, which causes inefficient charge transfer. The environment may further cause the electrocatalyst to be substantially less active, thus increasing the overpotential by that amount. Hence, the interface between photoelectrode and catalyst is a key aspect, which ultimately

Table 2. Performance of representative nanowire photoelectrodes toward solar fuel production. KP_i, potassium phosphate buffer; NWs, nanowires; μWs, microwires; NPs, nanoparticles.

Structure	*J* (mA cm^{-2})	*E* (V versus RHE)	FY (%)	Product	Bandgap (eV)	Onset (V versus RHE)	Stability (hours)	Conditions	Reference
Photocathodes: H_2 evolution									
Si NWs|MoS_2 nanosheets	16.5	0		H_2	1.1	0.26	48	1 sun, 0.5 M H_2SO_4, pH 0.5	(*81*)
Au|Cu_2O NWs|Ga_2O_3|TiO_2|RuO_x	~10	0	–	H_2	2	1	120*	1 sun, 0.5 M Na_2SO_4, 0.1 M NaPi, pH 5	(*77*)
Si|GaN NWs|Pt	38	0	~100	H_2	1.1	0.56	3000	1 sun, 0.5 M H_2SO_4, pH ~0	(*76*)
Photocathodes: CO_2R									
InP|TiO_2|Cu NPs	6.5	−0.6†	76.9	H_2	1.43	~−0.1†	12	λ = 532 nm, CO_2 saturated 0.5 M KCl	(*211*)
			8.7	CH_3OH					
n^+p-Si|GaN NWs|Sn NPs	−17.5	−0.53	20	H_2	1.1	0	10	1 sun, 0.1 M $KHCO_3$	(*212*)
			5	CO					
			76.9	HCOOH					
Cu_2O|SnO_x	−3.7	−0.35	16.1	H_2		~−0.1	12	2 sun, λ > 420 nm, 0.5 M $NaHCO_3$	(*113*)
			74.22	CO					
			6.08	HCOOH					
n^+p-Si μWs|Cu	−20.8	−0.44	55.5	H_2	1.1	~0.15	48‡	1 sun, 0.1 M $KHCO_3$, pH 6.8	(*69*)
			9.5	CH_4					
			10.5	C_2H_4					
n^+p-Si NWs|Cu NPs	~−10	−0.5	55.9	H_2	1.1	~0.05	50	1 sun, 0.1 M $KHCO_3$, pH 6.8	(*111*)
			7.5	HCOOH					
			3.1	CO					
			4.4	CH_4					
			24.3	C_2H_4					
			3.1	C_2H_5OH					
			3.9	C_3H_7OH					
Photocathodes: biologic systems									
Si NWs/*S. ovata*	~−0.2	0.14	82	CH_3COOH	1.1	0.26	130	1 sun, 20% CO_2/80% N_2 purged, brackish H_2O, pH 6.3 to 6.7	(*72*)
Photoanodes									
TiO_2 NWs|ALD TiO_2	1.1	1.5	–	O_2	3.0-3.2	0.1	–	1 sun, 1 M NaOH	(*119*)
WO_3 nanorods	2.26	1.23	–	O_2	2.61	0.5	–	1 sun, 0.5 M Na_2SO_4	(*124*)
$BiVO_4$|FeOOH|NiOOH nanoworms	4.5	1.23	>90	O_2	2.4	0.2	48	1 sun, 0.5 M KP_i, pH 7	(*121*)
Sn:Fe_2O_3 NWs	3	1.6	–	O_2	2.2	0.8	–	1 sun, 1 M NaOH, pH 13.6	(*122*)
WO_3|W:$BiVO_4$ NWs	3.1	1.23	–	O_2	2.6/2.4	0.6	–	1 sun, 0.5 M KP_i, pH 8	(*140*)
Si|Fe_2O_3 NWs	0.89	1.23	–	O_2	1.1/2.2	0.6	–	1 sun, 1 M NaOH	(*142*)
Branched ZnO NWs|Au NPs	1.7	1.23	–	O_2	3.1	0.3	3	1 sun, 0.5 M Na_2SO_4, pH ~7.0	(*151*)

*0.5 V versus RHE. †V versus the normal hydrogen electrode (NHE). ‡−0.58 V versus RHE.

enables a successful system integration. This interfacing may take a variety of forms, from ligands allowing a homogeneous dispersion of Au_3Cu nanoparticles along nanowire arrays (*71*), to anchoring groups that attach molecular catalysts onto passivating oxide coatings, and nanogaps promoting microbial growth (Fig. 3).

The overpotential, selectivity, and turnover requirements can be further alleviated by introducing biologic systems such as enzymes or bacteria, which operate near the thermodynamic potential of a given reaction (*72*). These biocatalysts cover a wide range of stability, cost, and reaction scope (*73*). While enzymes degrade rapidly outside the cellular matrix and require complex purification steps, they often set a benchmark in terms of catalytic activity and product selectivity because of their low overpotentials and high turnovers surpassing those of inorganic catalysts. An understanding of their active sites can further provide guidelines for the synthesis of high-performance, bioinspired catalysts. On the other hand, bacteria stand out as robust catalysts for hybrid bioinorganic laboratory prototypes and even industrial processes (e.g., fermentation or biofuel production). Those bacteria cultures can be sustained over days and provide a complex range of products through metabolic cascade reactions. In this case, nanowires provide a high–surface area platform to grow bacterial colonies, which can conveniently attach through flagella or pili (*72*, *73*).

PEC PERFORMANCE OF NANOWIRES

Photocathodes

Hydrogen evolution

A great number of studies have looked into H_2 evolution using nanowire photocathodes (*74*–*76*). In terms of design, most photocathodes use silicon (*75*), III-V (*76*), or metal oxide semiconductors (*77*, *78*), which are directly interfaced to established H_2 evolution catalysts such as Pt (*75*, *79*), MoS_2 (*80*, *81*), and RuO_x (*77*), as well as Ni-containing (*77*, *82*, *83*) or Co-containing (*84*) compounds (see Table 2 and Fig. 4). While these catalysts can be deposited in the shape of nanoparticles (*75*, *82*), flakes (*81*), or conformal coatings, their effect on the overall photocurrent is similar, as their high current densities at overpotentials below 100 mV (*85*) ensure that light harvesting is the limiting step.

Overall, Si remains the most popular light absorber for nanowire PEC (*86*, *87*). The best Si nanowire electrodes display photocurrents plateauing above 30 mA cm^{-2} (*67*, *81*, *88*, *89*) and an onset potential of around 0.4 to 0.5 V versus RHE (Fig. 4A) (*67*, *82*, *90*). To attain these values, photocathodes often use n^+p-Si wire arrays (*67*, *90*), whereas p-Si arrays are limited to photocurrents of only 10 to 20 mA cm^{-2} and onset potentials for proton reduction of 0.1 to 0.3 V versus RHE (*67*). These buried junctions decoupling the photovoltage from the band bending at the semiconductor-liquid interface can also be obtained using TiO_2 coatings, which have an additional role as passivating layers (*80*).

A higher photovoltage can be obtained using III-V semiconductors such as GaN (*76*, *91*, *92*), GaP (*56*), GaAs (*93*), InP (*94*, *95*), and InAs (*96*), which translates to an onset potential of 0.5 to 0.6 V versus RHE for H_2 evolution (Fig. 4C). In those cases, TiO_2 coatings can be again used as protective interfaces between the semiconductor and catalyst, which facilitate charge extraction and increase the electrode stability under operation (*93*, *94*, *96*). Accordingly, GaAs|TiO_2|Pt photocathodes sustained a photocurrent density of −11 mA cm^{-2} over 67 hours at −0.6 V versus RHE, whereas unprotected electrodes were completely degraded after 36 hours of

Table 3. Comparison between the performance of nanowire PEC systems for unassisted solar fuel production.

Structure	*J* (mA cm^{-2})	FE (%)	Product	STF (%)	Stability (hours)	Conditions	Reference
Photochemical diodes							
Si/TiO_2 nanotree			H_2, O_2	0.12	4.5	1.5 sun, 0.5 M H_2SO_4	(*35*)
Ru/Rh-$SrTiO_3$–$BiVO_4$ mesh			H_2, O_2	0.0017	18	450 W Xe lamp, $\lambda \geq 400$ nm, H_2SO_4, pH 3.5	(*34*)
Double-band p-GaN/p-$In_{0.2}Ga_{0.8}N$			H_2, O_2	~1.8 (H_2)	10	~26 sun, H_2O, pH ~7.0	(*159*)
Wired PEC							
InP-$BiVO_4$ (side by side)	0.41 ± 0.02		H_2, O_2	0.5	0.75	1 sun, 1 M KP_i, pH 7	(*94*)
p-Si nanoarray|Pt-Mo:$BiVO_4$|CoPi	0.46	100*	H_2, O_2	0.57	3.5	1 sun, 0.1 M KP_i, pH 5.5	(*156*)
Au|Cu_2O|Ga_2O_3|TiO_2|RuO_x-$BiVO_4$|CoPi	~2.4	~100	H_2, O_2	~3	12	1 sun, 0.2 M KB_i, pH 9.0	(*77*)
Biophotochemical diodes							
Si/*S. ovata*–TiO_2	0.35	86 ± 9	CH_3COOH, O_2	0.38	130	1 sun, 20% CO_2/80% N_2 purged, brackish H_2O, pH 6.3 to 6.7	(*72*)
		52	PHB	0.2		(+*E. coli*)	
Si/*S. ovata*–Si multi-jn PV–Pt	~0.65	~80	CH_3COOH	~3.6	168	0.25 sun, 20% CO_2/80% N_2 purged, phosphate-enhanced medium, pH 6.4	(*161*)

*Assumed.

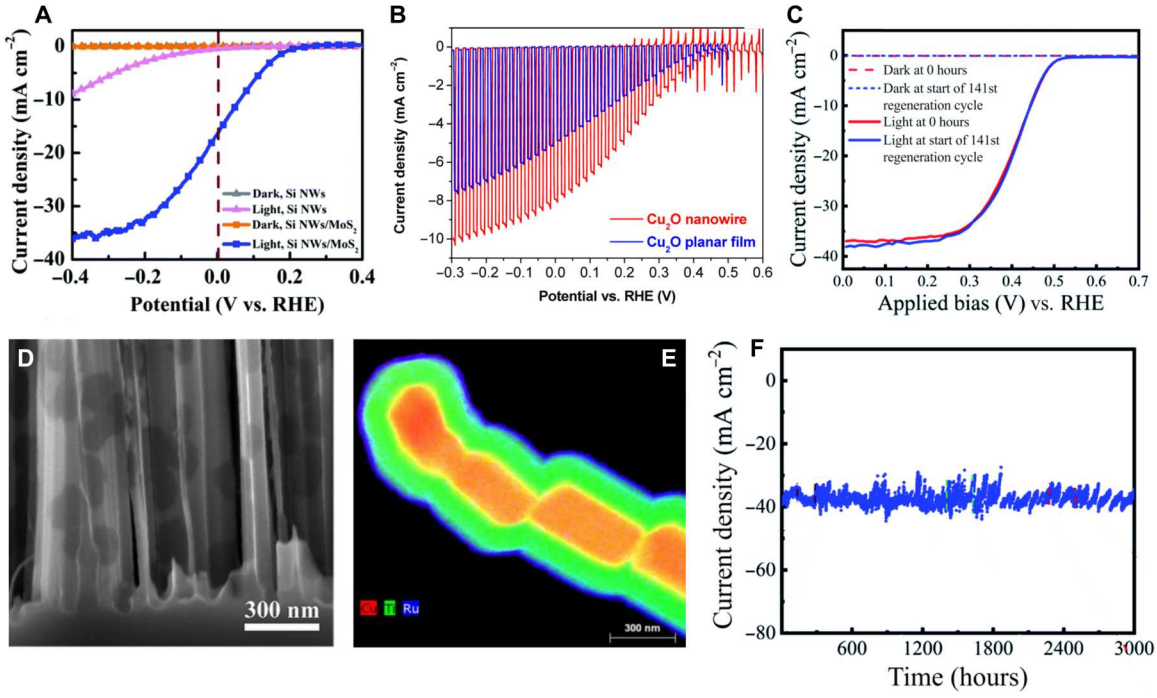

Fig. 4. Examples of nanowire photocathodes for H_2 evolution. (**A** and **D**) Si nanowires (NWs) with a MoS_2 catalyst, reproduced with permission from Hu *et al.* (*81*). (**B** and **E**) Performance of multilayered, heterojunction Cu_2O photocathodes, reproduced with permission from Luo *et al.* (*97*). (**C** and **F**) Long-term stability of a GaN|Pt photocathode, adapted with permission from Vanka *et al.* (*76*).

operation (*93*). A similar way of improving the onset potential and photocathode stability is by surface modification of the nanowires (*92*, *95*). Sulfur-dissolved oleylamine was used to produce an inorganic, protective sulfide coating onto InP nanowires (*95*), whereas an organic 1,2-ethanedithiol enhanced the carrier lifetime by suppressing chemisorbed —OH and —O bonds at the GaN nanowire surface (*92*). However, the highest stability was reported using a n^+-p Si|n^+-GaN nanowires|Pt photocathode, which could operate in 0.5 M H_2SO_4 under 1-sun irradiation for 3000 hours (see Fig. 4F and Table 2) (*76*).

The onset potential can be further increased beyond 0.6 V versus RHE for H_2 evolution using Cu_2O (*97*) or CuO (*98*–*100*) nanowire photocathodes. However, Cu_2O undergoes photodegradation in water; therefore, a careful surface passivation is required (Fig. 4E). This is typically achieved using wide-bandgap metal oxide coatings including TiO_2, ZnO (*100*), or NiO_x (*101*), which act as electron-selective layers facilitating charge separation. A careful choice of materials can improve the band alignment between the conduction band level of the light absorber and that of the electron-selective layer, reducing photovoltage losses. Accordingly, the onset potential of Cu|Cu_2O|AZO|TiO_2|RuO_x nanowire heterojunction photocathodes could be shifted from 0.6 to 1 V versus RHE, by replacing the aluminum-doped zinc oxide (AZO) coating by a Ga_2O_3 layer (*77*, *97*). The fill factor of the electrode could be further improved by adding a hole-selective layer between a Au metal substrate and Cu_2O, which improves the overall fuel production in a bias-free tandem configuration (*78*), as we discuss later in more detail.

CO_2 reduction

Another reaction of interest to realizing artificial photosynthesis is the photoelectrochemical conversion of CO_2 into value-added chemicals (Fig. 5). While the redox potentials for CO_2R reactions (e.g., $E_{CO_2/CO}$ = −0.11 V versus RHE and E_{CO_2/C_2H_4} = 0.08 V versus RHE) are similar to that of the hydrogen evolution reaction (HER; E_{H_2O/H_2} = 0 V versus RHE), the complexity of the reaction kinetics for CO_2 activation and conversion often results in needing large overpotentials to drive the reaction. In addition, reaction selectivity is essential, as there is competing HER, as well as the broad scope of products that are produced from CO_2R (*102*). Unlike HER where a monolayer of Pt is sufficient to drive appreciable currents (*75*), CO_2R catalysts often require large catalytic surface areas to achieve similar currents at modest overpotentials. To further add a layer of complexity, accessing and selecting multicarbon products are an interplay between the current density and driving potential (*103*).

The necessity of using high–surface area catalysts for CO_2R leads to the problem of parasitic light absorption when using planar systems. An earlier work showed that the optical transmittance of a copper film was 0% at a thickness of 100 nm, which only increased to 15% when decreasing the thickness to 35 nm. However, decreasing the thickness changed the selectivity toward methane from 60 to 0% due to the grain boundary oxidation of a thinner film (*104*). To overcome these limitations, various strategies have been used such as catalyst patterning to allow light transmission or direct irradiation, back-side illumination through conductive glass substrates, or choosing a photocathode material that also has catalytic activity. Patterning the substrate to selectively deposit the catalyst on portions of the surface allows light to pass through exposed areas, but this only slightly mitigates the problem as the photocurrent density is still usually reduced by ~50% (*104*, *105*). Another method is the use of a metal prism array or dielectric nanocone structure to direct

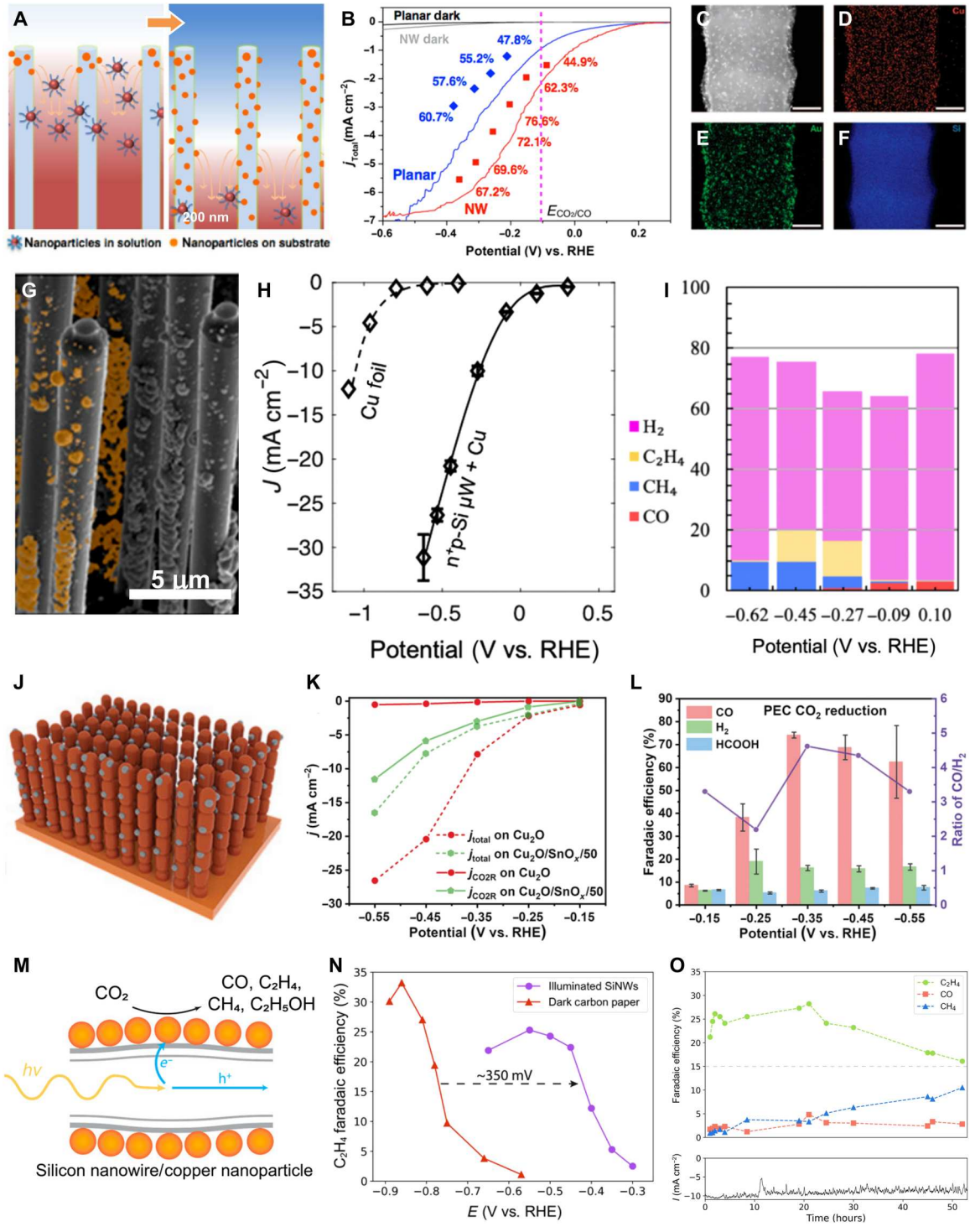

Fig. 5. Nanowire photocathodes for CO_2R. (**A** to **F**) Au_3Cu nanoparticles assembled on Si nanowire arrays, reproduced with permission from Kong *et al.* (*71*). (**A**) Schematic of the nanoparticle deposition; (**B**) linear sweep voltammetry (LSVs) and faradaic efficiencies toward CO production; and (**C** to **F**) SEM and corresponding elemental mapping of Cu (D), Au (E), and Si (F). Scale bars 200 nm. (**G** to **I**) Si|Cu photocathodes for multicarbon production, reproduced with permission from Kempler *et al.* (*69*). (G) False-color SEM image and (H and I) PEC performance. (**J** to **L**) $Cu_2O|SnO_x$ photocathode, reproduced with permission from Zhang *et al.* (*113*). (J) Schematic depiction and (K and L) PEC activity. (**M** to **O**) Cu nanoparticles on Si nanowires for selective ethylene synthesis, reproduced with permission from Roh *et al.* (*111*). (M) Schematic of the Si nanowire/Cu nanoparticles assembly, (N) faradaic efficiencies, and (O) stability test.

the incoming light to maximize transmittance, but this limits the area of catalyst coverage and catalyst options, which leads to generally the need for large overpotentials (*106*, *107*). Choosing a photocathode that acts as the catalyst removes these considerations altogether but greatly limits materials selection, and such a photocathode remains to be discoveredfor selective aqueous CO_2R.

On the other hand, the unique structure of nanowire photoelectrodes bypasses these limitations and shows greater light absorption instead due to its enhanced light trapping properties as described earlier. When comparing the same mass loading of Au_3Cu nanoparticles on planar Si and Si nanowires for CO_2 conversion to CO, it was found that the total photocurrent was larger for the nanowire system over the planar system (Fig. 5, A and B) (*71*). This was also seen for a silicon microwire system where a large mass of Cu (330 μg cm^{-2}) was photoelectrodeposited onto the wires but was still able to generate a photocurrent of over 30 mA cm^{-2} under 1-sun illumination (Fig. 5, G and H) (*69*). On a planar substrate, this would correspond to a film thickness of approximately 370 nm where the expected optical transmittance is 0%.

Catalysts deposited onto nanowire photoelectrodes also see a lower onset potential and a higher selectivity toward the desired CO_2R product despite generally having a smaller photovoltage than their planar counterparts. For example, for CO_2R to CO, a planar InP photocathode covered with TiO_2 and Au showed a current density of 2 mA cm^{-2} at −0.11 V versus RHE while etching the InP into a nanopillar array increased it to 4.53 mA cm^{-2} at the same potential. Along with the increase in current density, the faradaic efficiency toward CO also increased from 53.2 to 84.2%, which corresponds to an almost fourfold increase in partial current density toward CO production (*61*). This was also seen when using nitrogen-doped graphene quantum sheets onto Si photoelectrodes, where the onset potential shifted positively by 250 mV when using nanowires instead of a planar substrate and the faradaic efficiency toward CO increased from 90 to 95% (*108*). Similar effects were observed for CO_2R to $HCOO^-$ using photoelectrodeposited tin nanoparticles on Si. The faradaic efficiency toward formate was improved from 33% on planar Si to 40% on Si nanowires, while the total production of formate was increased fivefold (*109*). The origin behind this shift in onset potential and increased selectivity has not been fully explored and has been often attributed to superior light absorption, but this would only explain short-circuit currents and not currents within catalytically limited regimes. We can draw from studies done in the electrochemical CO_2R community and best attribute these benefits to increased surface area of the catalyst and an increase in pH within the wire network to suppress HER (*110*).

These effects become more pronounced when reducing CO_2 further into multicarbon products such as ethylene, ethanol, and propanol. At low mass loadings of 5 μg cm^{-2} of 7 nm Cu nanoparticles on Si nanowires, the CO:C_2H_4 ratio is 3:1 at −0.5 V versus RHE but changes to 1:8 when increasing the mass loading to 40 μg cm^{-2} and reaches a faradaic efficiency toward C_2H_4 of 24.3% (*111*). This was attributed to the necessity of building up intermediates to access multicarbons, which occurs with more surface area. On the other hand, when copper was interfaced to planar silicon photocathodes at low mass loadings to prevent parasitic light absorption, the faradaic efficiency toward C_2H_4 could only reach 6% and mostly favored single-carbon products across all potential ranges (*112*).

Interestingly, nanowire photoelectrodes also see enhanced stability for CO_2R over their planar counterparts despite the nanowires generally introducing surface states that often lead to failure modes. During cycling, planar p-Si underwent a gradual deactivation within 5 cycles, while the nanowires did not. This was attributed to nanowires having a hydrogen- or fluorine-functionalized surface from etching that prevented oxidation (*109*). However, in a different work, x-ray photoelectron spectroscopy data showed a notable increase in the SiO_2/Si ratio on silicon nanowires after 1 hour, although it sustained stable CO_2R for over 50 hours, suggesting that prevention of oxide growth may not be the reason behind its stability (Fig. 5O) (*111*). Furthermore, a TiO_2-covered InP nanopillar array saw improved stability toward methanol production over its planar counterpart despite both having passivation layers to protect the surface (*61*), while SnO_x-modified Cu_2O nanowires sustained almost 80% faradaic efficiency toward CO for 11 hours (Fig. 5, J to L) (*113*). Another possible reason for this stability could be the nanowire morphology, which is better able to prevent delamination of the catalyst from the surface than in flat substrates (*69*).

Investigations into the charge transfer between photocathode and catalyst may help elucidate the reasons behind the benefits of using nanowire photoelectrodes for CO_2R, such as lower onset potentials, higher selectivity, and increased stability. This effect becomes prominent when using molecular catalysts where the orientation or the catalyst/surface interaction is a key consideration. When using $[Ni(bpy)_2]$ as a catalyst, the nanowires resulted in a 300 mV lower onset potential for CO_2R over a planar Si substrate. The team concluded that improved light harvesting would fail to account for such difference in potential and suggested that this discrepancy was caused by a difference in charge transfer. Because nanowires are multifaceted, while planar silicon only has one facet exposed, the electron transfer pathways are likely formed on Si nanowire/$[Ni(bpy)_2]$ interfaces that favor the process (*114*).

Biological systems such as bacteria have also been used as catalysts because of their ability to accept charges from semiconductor surfaces and their excellent selectivity at low overpotentials (*115*). The same considerations above for CO_2R mean that bacteria have often been used for dark cathodes because of their low optical transmittance (*116*) but exemplify that nanowires are an excellent substrate for forming these biohybrid interfaces. In addition, single-cell level imaging showed that *Shewanella oneidensis* MR-1 can recognize and show preferential attachment to nanowires (*117*). As a result, *Sporomusa ovata* has been interfaced to silicon nanowire photocathodes to reduce CO_2 into acetate with a faradaic efficiency up to 90% for 200 hours. Although *S. ovata* can only catalyze CO_2 under anaerobic conditions, stable CO_2R was demonstrated under aerobic conditions when Pt was added because of mass transport maintaining anaerobic conditions within the wire assembly (*72*). This demonstrates a unique feature of the nanowires, which can create and maintain a different environment from the bulk conditions playing a role in many catalytic reactions.

Photoanodes

In terms of oxygen evolution, transition metal oxides remain the most encountered photoanode materials. The wide bandgaps of 2.5 to 3.5 eV are accountable for their robustness under operation, which can span up to several weeks for oxide nanostructures in aqueous electrolytes (see Table 2) (*41*, *118*). The performance is

enhanced in case of the nanowires because of their light trapping and scattering effect. For example, while TiO_2 films are often transparent, the photocurrent density of TiO_2 nanowire array electrodes could be improved from 0.125 to 0.73 mA cm^{-2} at 1.5 V versus RHE by increasing the nanowire length from 0.28 to 1.8 μm (*119*). However, a wider bandgap also restricts the amount of light that can be harvested over the visible spectrum. To address this challenge, several strategies have been explored including doping, building core-shell heterojunctions, and nanowire sensitization (Fig. 6).

While nanowire photoanodes including TiO_2 and ZnO absorb mostly in the ultraviolet (UV) region, other oxides including WO_3 (*120*), $BiVO_4$ (*121*), and Fe_2O_3 (*122*) extend their absorption in the visible spectrum (Table 2). However, even those suffer from low photovoltages, which may be due to a high recombination, low charge carrier mobility, or noncontributing excitations (*9*, *123*). Therefore, WO_3 only displays an onset potential of 0.5 to 0.7 V versus RHE for oxygen evolution (*51*, *124*), whereas the 0.8 to 1.0 V versus RHE onset of hematite (*125*–*127*) is even more positive. Hence, one strategy is to dope wide-bandgap oxides with atoms such as nitrogen, carbon, tin, or titanium.

N doping of TiO_2 not only increases the incident photon to current efficiency (IPCE) in the UV region but also shifts the light adsorption to higher wavelengths (Fig. 6, A and E) (*128*, *129*). For example, the IPCE of TiO_2 nanowire photoanodes with a cobalt oxygen evolution catalyst (OEC) was increased from around 60% to above 80% by N doping, while the IPCE spectrum of doped samples already showed activity at 500 nm irradiation (*129*). While doping in itself decreased the photocurrent density of TiO_2 (from 0.38 to 0.23 mA cm^{-2} at 1.23 V versus RHE) and shifted the onset potential positively (from 0.2 to 0.5 V versus RHE), the Co OEC addition achieved the highest photocurrent of 0.61 mA cm^{-2} at 1.23 V versus RHE for doped samples (*129*). Similarly, the IPCE of ZnO nanowire arrays could be improved from ~40% to over 80%, whereas the IPCE onset shifted from roughly 400 to 450 nm, resulting in a photocurrent density of 0.4 mA cm^{-2} at 1.0 V versus Ag/AgCl (*130*). On the other hand, tetravalent atoms such as C or Sn have been shown to increase the IPCE of TiO_2 in the UV range without shifting the absorption onset (*128*, *131*). Hydrogen treatment has been further used to reduce Ti^{4+} to Ti^{3+} species, yielding dark TiO_2 nanowire photoanodes with IPCE values approaching 100% at wavelengths below 400 nm (*131*–*133*).

In case of hematite, Ti (*31*) and Sn (*122*, *134*) have been used as dopants. Although no notable shifts were observed in the onset potentials, these treatments did produce photocurrent densities as high as 1 mA cm^{-2} for Ti:Fe_2O_3 (*31*) and 3 mA cm^{-2} for Sn:Fe_2O_3 (*122*) at 1.6 V versus RHE, as opposed to the photocurrents around 0.2 mA cm^{-2} of undoped samples at the same potential. The formation of oxygen vacancies and Fe^{2+} through β-FeOOH decomposition in an oxygen-deficient environment provided a similar effect, resulting in a photocurrent of 3.37 mA cm^{-2} at 1.5 V versus RHE (*135*).

Another route to increase the performance of nanowire photoelectrodes is by making core-shell structures (Fig. 6, B, C, F, and G). In this design, the shell may act as a catalyst (*136*), passivating layer (*137*), or heterojunction improving charge separation (*138*, *139*). For example, a W-doped $BiVO_4$ coating increased the photocurrent of a WO_3 nanowire photoanode from 1.1 to 3.1 mA cm^{-2} at 1.23 V versus RHE, even in the absence of a dedicated OEC (*140*). Core-shell heterojunctions can also consist of two (*140*) or more (*141*) complementary light absorbers, which are able to harvest a larger portion of the solar spectrum. For instance, the onset potential of hematite for O_2 evolution could be shifted ~0.4 V earlier by depositing Fe_2O_3 onto Si (*142*). The shells themselves can be further nanostructured, thereby maximizing light absorption and the photoactive surface area. These branched nanowires have been previously demonstrated by growing TiO_2 nanorods onto Si nanowire

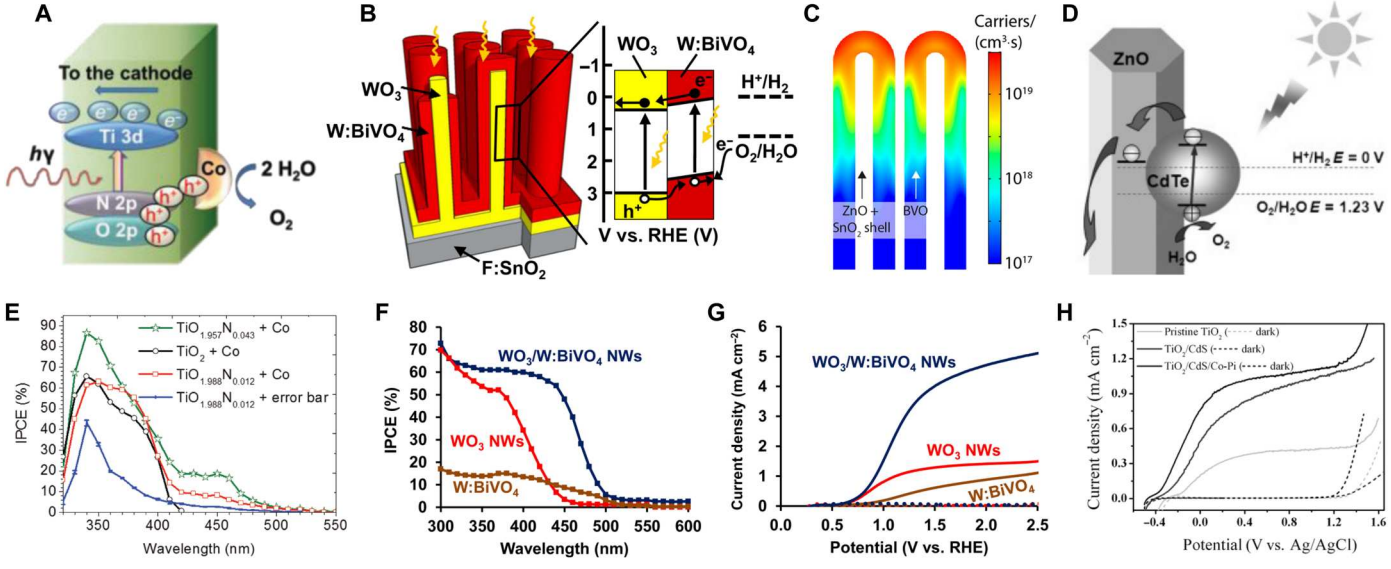

Fig. 6. Strategies to improve the performance of nanowire photoanodes. (**A** and **E**) Doping of TiO_2 photoanodes and corresponding IPCE spectra (E), reproduced with permission from Hoang *et al.* (*129*). (**B**, **C**, **F**, and **G**) Core-shell nanowire heterojunctions. (B, F, and G) WO_3|$BiVO_4$ electrode with corresponding IPCE spectra (F) and LSV plots (G), reproduced with permission from Rao *et al.* (*140*). (C) ZnO|SnO_2|$BiVO_4$ nanowire array, reproduced with permission from Bielinski *et al.* (*139*). (**D**) Sensitization of ZnO nanowires with CdTe quantum dots, reproduced with permission from Chen *et al.* (*146*). (**H**) LSV traces of TiO_2 sensitized with CdS, reproduced with permission from Ai *et al.* (*145*).

array backbones (*143*) or by growing ZnS nanowires onto ZnO rods (*144*).

Sensitization is another popular alternative to increase the light absorption of oxide photoanodes (Fig. 6, D and H). In this case, quantum dots of II-VI semiconductors such as CdS (*145*), CdTe (*146*), or CdSe (*147*, *148*) are deposited onto TiO_2 or ZnO nanowires. Water oxidation catalysts such as Co-Pi can again improve the photoanode onset potential and fill factor (*145*), whereas additional heterojunctions with light absorbers such as Cu_2O have recently proved beneficial, yielding very early onset potentials below −1.0 V versus RHE (*149*, *150*). Alternatively, TiO_2 and ZnO nanowires can be decorated with Au nanoparticles, which achieve a broadband UV-visible absorption through plasmonic effects (*151*, *152*).

Besides the material choice and fabrication methods, the photocurrent and onset potential can also be adjusted by depositing suitable oxygen evolution reaction (OER) catalysts. IrO_2 and RuO_2 have been established for water electrolysis, providing overpotentials of 0.3 to 0.4 V for O_2 evolution in strongly acidic or alkaline media (*153*). These noble metal catalysts can also be used for photoanodes (*154*), resulting, for example, in improved fill factors and early onset potentials of 0.2 V versus RHE for TiO_2 nanowire photoanodes (*35*). However, as described earlier, earth-abundant catalysts including Co, Fe, or Ni compounds are more popular for PEC applications, where reactions are often conducted under (near) neutral pH, at current densities below 10, or even 1 mA cm^{-2} (*85*).

Overall systems

As established earlier, two complementary light absorbers are often required for overall fuel production. These systems can span a wide range of designs, from planar, buried junction tandem devices (*41*), to two-electrode tandem PEC devices (*2*), and Z-scheme photocatalyst sheets with solid mediators (*155*). Hence, a number or nanowire-based designs can be envisioned, including the nanowire photochemical diode (Fig. 7). While the concept of nanowire photochemical diodes, as depicted in Fig. 1C and proposed by Nozik, is challenging to implement in practice, other related systems can operate similarly (Table 3). Namely, these systems provide a single optical light path, take the macroscopic shape of a panel, and consist of two semiconductors of different bandgaps, which are interfaced either directly or through an ohmic contact.

A first category involves wired PEC systems for overall water splitting. In this case, a photoanode can be wired to a photocathode in an overlapping, single light path (tandem) or side-by-side arrangement. Electrodes are often facing the light source to make use of the light trapping advantages of the nanowire geometry. For example, appropriate catalysts result in earlier onset potentials for Si nanowire photocathodes (0.45 V versus RHE) and $BiVO_4$ photoanodes (0.3 V versus RHE), resulting in an overlap at 0.38 V versus RHE, with a steady-state STH efficiency of 0.57% for the corresponding tandem PEC device (*156*). The overlap can be improved by introducing photocathodes with early onset potentials, such as the Cu_2O nanowire heterojunction electrodes. Their onset potential of 1 V versus RHE shifts the operating potential of Cu_2O-$BiVO_4$ tandem devices to around 0.6 V versus RHE, resulting in a 3% STH efficiency (*77*). A side-by-side arrangement is beneficial if the electrodes are deposited on opaque substrates or if the light absorption and scattering through the first semiconductor is too strong. However, care must be taken when calculating the STF efficiency, as the geometric areas of both light absorbers add up in a two–optical path configuration (*94*, *157*).

Photocatalyst systems, where no charges are flowing through an external circuit, are closer to Nozik's photochemical diode design from Fig. 1C. In this case, semiconductors can be interfaced either directly, forming heterojunctions (*158*) and ohmic contacts (*35*), or via solid-state conductive mediators such as ITO nanoparticles (*155*). This contact between nanowires becomes particularly important because a limited contact area, insufficient charge separation, or charge recombination at the interface can substantially decrease the overall fuel production. For instance, an eightfold decrease in the rates of H_2 and O_2 evolution was observed when replacing a mixed Ru/Rh-$SrTiO_3$–$BiVO_4$ nanowire mesh with the corresponding bilayer mesh (Fig. 7A). For the latter, only nanowires in the vicinity of the Ru/Rh-$SrTiO_3$–$BiVO_4$ layer interface contributed to the charge separation and subsequent fuel production (*34*). One way of avoiding parasitic contact losses is by growing nanowire structures directly on top of each other. Accordingly, a 0.12% STH efficiency was obtained by partly covering Si rods with TiO_2 nanowires in a so-called nanotree heterostructure. In this configuration, UV light is used by TiO_2 for O_2 evolution, whereas the visible light is transmitted to the exposed Si wire underneath for proton reduction (Fig. 7C), fulfilling the requirements of a single light path (*35*). A similar strategy could be applied to other types of heterostructures, e.g., the growth of CdS nanowires on $BiVO_4$ platelets for overall water splitting (*158*). This nanowire photochemical diode could be further integrated by introducing heterojunctions along a single nanowire. Accordingly, p-GaN/p-$In_{0.2}Ga_{0.8}N$ nanowires, where the two light absorbers have bandgaps of 3.4 and 2.6 eV, were estimated to reach a ~1.8% STH efficiency under ~26-sun irradiation (*159*).

As noticeable from the previous examples, most systems are limited to overall water splitting because additional overpotentials of several hundred millivolts occur for CO_2R (*160*). However, these limitations can be overcome using biologic systems operating at very low overpotentials, close to the standard electrode potentials. Taking advantage of an overpotential <200 mV of the bacterium *S. ovata*, a Si-TiO_2 nanowire PEC tandem was able to perform unassisted acetate production at a 0.38% STF efficiency and faradaic efficiency up to 90%. The versatility of this approach toward making higher-value multicarbon products was demonstrated by feeding the acetate to a genetically engineered *Escherichia coli*. This bacterium could convert the acetate to *n*-butanol, polyhydroxybutyrate (PHB) polymer, and different isoprenoid natural products via acetyl–coenzyme A (CoA), attaining a 0.20% overall STF efficiency for the PHB synthesis (*72*). More recently, a close packing of *S. ovata* bacteria onto conductive Si nanowire arrays resulted in an STF of 3.6% for acetate production, when driving the process by an externally wired, multijunction Si PV cell (*161*).

The performance of nanowire systems also depends on their integration into suitable photoreactors. On a macroscopic level, these nanowire electrodes and the corresponding tandem devices are solid plates, which makes their setup and operation similar to those of other PEC systems (*2*). Normally, photoelectrodes as those depicted in Fig. 1 (A and B) can be operated in two-compartment cells, where ion-selective membranes separate the two compartments avoiding product crossover. In case of the proposed nanowire diode (Fig. 1C), the ohmic contact would provide a physical separation between the two sides of the diode, which results in

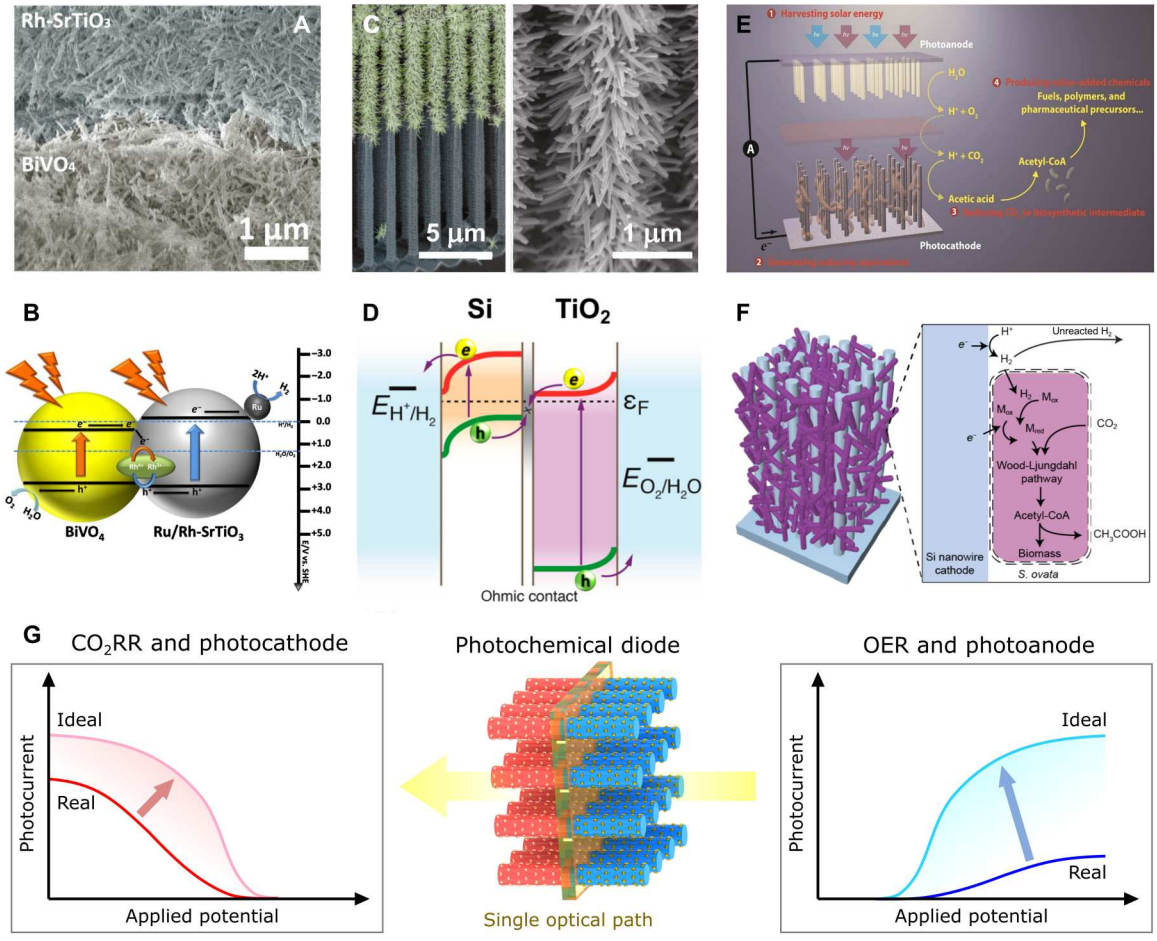

Fig. 7. Nanowire PEC systems for overall solar fuel production. (**A** to **D**) Nanowire photochemical diodes for water splitting. (A and B) Bilayer Ru/Rh-$SrTiO_3$–$BiVO_4$ nanowire mesh, reproduced with permission from Liu *et al.* (*34*). (C and D) Si/TiO_2 nanotree, adapted with permission from Liu *et al.* (*35*). (A and C) False color: SEM images. (B and D) Energy schemes. (**E** and **F**) Bacteria-nanowire interfaces for light-driven acetate production. (E) *S. ovata* bacteria are interfaced to a Si nanowire electrode. Unassisted acetate production is performed by wiring the Si nanowire photocathode to a TiO_2 photoanode, reproduced with permission from Liu *et al.* (*72*). (F) Wood-Ljungdahl pathway for acetate production within an *S. ovata* bacterium, adapted with permission from Su *et al.* (*161*). (**G**) Efficient nanowire photochemical diodes require further development on the light harvesting and catalysis sides. A positive shift in the cathodic signal can be obtained by using catalysts with lower overpotentials for CO_2RR and HER or photocathodes providing higher photovoltages and photocurrent outputs. Similar effects can increase the activity of a photoanode on the OER side. A suitable integration of the oxidative and reductive sides in a single–optical path system is required to maximize light absorption.

overpotentials due to pH gradient buildup. This can be avoided by using strongly basic or acidic electrolytes. Under neutral conditions, these nanowire diodes would require flow systems with separators (*162*, *163*) or integrated membranes (*157*) to prevent product crossover while maintaining an even pH distribution. Alternatively, the diodes could simply operate in a one-compartment reactor. The resulting explosive product mixtures can be filtered using gas-separating membrane units, as demonstrated recently for large-scale photocatalyst sheets (*164*).

SEMICONDUCTOR CHARGE TRANSFER

While considerable efforts have been made in terms of nanowire geometry and synthesis, doping, heterogeneous layers for passivation or band alignment, catalyst discovery and integration, or semiconductor material discovery, a fundamental goal is to articulate correlations between each of these components and the overall PEC performance: mainly, onset potential, photocurrent, selectivity, and stability. Understanding charge transfer through these multicomponent systems can further inform the design of efficient PEC devices. For instance, there was a positive shift of 300 mV using $[Ni(bpy)_2]$ (*114*) and 230 mV using [Co(TPA)Cl]Cl (*165*) on silicon nanowires compared to planar Si for PEC CO_2R, which was attributed to the multifaceted nature of the silicon nanowires, allowing for more efficient charge transfer. Those charge carrier dynamics in photoelectrochemical diodes span a wide extent of time scales. Charge migration or transfer after photoexcitation occurs on femtosecond to picosecond time scales (*166*). Depending on the degree of charge separation and extraction, recombination rates occur on nanosecond to millisecond time scales (*167*), while surface reactions span millisecond to second time scales depending on the kinetics of the reaction. The most prevalent techniques that have been used to study charge transfer are electrochemical

impedance spectroscopy (EIS) and transient absorption, as described below.

EIS using an alternating current measures the current response to a sinusoidal potential perturbation as a function of frequency and can be used to differentiate sources of overpotentials that may be difficult to detangle otherwise. It is a powerful technique that examines frequency-dependent processes such as charge transfer and diffusion but requires careful analysis and knowledge of the system to use representative equivalent circuits (*168*, *169*). Most often for (photo)electrochemical systems, EIS is used as a supporting technique to confirm differences in activity. For example, in a CdS nanowire system decorated with Ni_3S_2 for water reduction, the optimal molar ratio was found to be 1:10 for Ni_3S_2 to CdS. The Nyquist plots from EIS revealed that this molar ratio gave the smallest charge transfer resistance under illumination when Ni_3S_2 was interfaced with CdS. However, the resistance was larger than pure Ni_3S_2 by three orders of magnitude, showing that the enhanced activity comes from a better charge extraction from the CdS (*170*). In addition, EIS also helped explain how dual-etching TiO_2 and doping with W enhanced the photocurrent by 225%. By creating a Mott-Schottky plot, flat-band potentials and charge carrier densities were extracted from the EIS data. The dual-etched–doped TiO_2 exhibited a higher flat-band potential of −0.60 V versus Ag/AgCl and a larger charge carrier density of 5.04×10^{18} cm^{-3}, while the pristine TiO_2 had a lower flat-band potential of −0.89 V versus Ag/AgCl and a lower charge carrier density of 3.86×10^{18} cm^{-3}. The higher flat-band potential facilitates more efficient charge transfer, while the charge carrier density leads to a larger photocurrent (*171*).

Another powerful alternative to elucidate charge transfer is by looking at excited state lifetimes through transient absorption. Charge transfer processes are on the order of femtosecond to picoseconds, which makes ultrafast spectroscopy a candidate for measuring their kinetics. Transient absorption probes charge carrier dynamics by applying a pump to photoexcite the electrode and measuring the change in absorption over time. In the CdS/Ni_3S_2 example above, the impedance spectroscopy was complemented by ultrafast transient absorption spectroscopy to get a clearer understanding of why the 1:10 molar ratio of Ni_3S_2 to CdS ratio had the best performance. The average lifetime of the excitons for pure CdS was calculated to be 686 ps but decreased to 185 ps with the addition of 10% Ni_3S_2. However, upon further addition of Ni_3S_2, the average lifetime increased to 461 ps. This was attributed to the intimate contact of the Ni_3S_2 and the fast transfer of charges to Ni_3S_2 from the CdS. On the other hand, further increasing the molar ratio to 3:10 led to the formation of flocculent structures that led to decreased contact with the CdS, resulting in increased lifetimes (*170*).

With the advent of core-level extreme UV (XUV) ultrafast transient spectroscopy, it is possible to get element-specific information while also probing electron and hole dynamics independently. Unlike UV, visible, or infrared spectroscopy, which has overlapping features from all the elements within the light path, XUV or x-rays are capable of core-to-valence transitions with a unique signature for each element (*172*). This technique was used to measure charge transfer kinetics in a Ni-TiO_2-Si junction by probing the Ti $M_{2,3}$ edge, Ni $M_{2,3}$ edge, and Si $L_{2,3}$ edge and found that the photogenerated hole travels ballistically through the 19 nmthick TiO_2 layer into the Ni on a femtosecond time scale. Afterward, the holes back-diffuse through the TiO_2 and recombine at the Si/TiO_2 interface on picosecond time scales (*173*). This confirms previous studies that saw thick layers of amorphous TiO_2 being used as passivation and transport layers without losses in conductivity (*47*, *57*).

In addition to these two more representative techniques, other unique approaches have been used to track charge transfer in photoelectrodes such as scanning electrochemical spectroscopy (*45*), single-particle photoluminescence spectroscopy (*174*), and Kelvin probe force microscopy (*175*). While offering important insights, these approaches are not readily generalizable to studying a wide range of photoelectrodes due to their setup. However, the development and advancement of all mentioned techniques will be crucial in gaining deep insights into the photoelectrochemical process and design.

OUTLOOK

As discussed above, a careful selection of the light absorbers and catalysts can substantially influence the performance of a nanowire PEC device toward solar fuel synthesis. These same criteria apply to the fabrication of efficient photochemical diodes. To achieve a sufficient overlap between the photocurrent traces of the photocathode and photoanode (Fig. 1D), stable photoelectrodes with high photovoltages and photocurrent outputs must be developed. These high photovoltages can be attained by either introducing new semiconductor materials or carefully designing the device structure. Earlier photoelectrochemical onset potentials can be further obtained by interfacing these light harvesters with newly discovered CO_2RR, HER, and OER catalysts, which display high selectivities at low overpotentials (Fig. 7G). Below, we investigate further strategies that may help maximize light absorption, photocurrent, and photovoltage.

In terms of photovoltage, ferroelectric materials can achieve open circuit voltages higher than the bandgap through the bulk photovoltaic effect. In these cases, charge separation occurs at domains oriented along the polarization direction. Accordingly, these materials do not require p-n junctions, as charges separate spontaneously. While this effect has been observed for $BiFeO_3$ crystalline films (*176*), similar effects are hypothesized to occur along ferroelectric perovskite nanowires such as $CsGeBr_3$ (*177*). Ferroelectric $BaTiO_3$ and $SrTiO_3$ shells have been demonstrated to alter the onset potential, photocurrent, and fill factor of TiO_2 nanowire photoanodes, depending on the poling direction (*138*, *178*).

An opportunity to enhance the photocurrent is given by plasmonics (*152*, *179*, *180*). In this case, Au or Ag nanoparticles are deposited on nanowire photoanodes such as TiO_2 or ZnO (*179*). This improves the kinetics of oxygen evolution and photoactivity due to the localized surface plasmon resonances and hot electron injection (*181*). While Au nanoparticles often enhance light absorption within the same wavelength range (*181*, *182*), a choice of different nanoparticle shapes (*152*) and electrode morphologies (*151*) can extend light absorption far within the visible region (*151*, *152*). This strategy stands out in the case of nanowire photoelectrodes,

as nanowires constitute an excellent scaffold to immobilize plasmonic nanoparticles at a greater loading without blocking light, resulting in notable enhancements in terms of light absorption.

A different approach to overall solar fuel production is offered by organic transformations (*183*–*186*). In this case, the thermodynamically demanding O_2 evolution (E_{H_2O/O_2} = 1.23 V versus RHE) can be replaced by organic oxidations, which already occur at lower applied potentials of 0.3 to 0.6 V versus RHE (*187*). This induces a negative shift in the oxidation curve, which improves the overlap, resulting in higher photocurrents under no applied bias voltage.

At last, to bring this technology closer to real-world applications, more focus needs to be placed on the high-throughput, scalable fabrication of stable nanowire PEC devices. While few reports have looked into the scalability of nanowire photoelectrodes (*15*, *188*), strategies have been recently proposed to improve stability (*76*, *189*). A self-passivation of the Si substrate to SiO_2 helps sustain the performance of a Si|nanowire GaAs|TiO_2|NiO_x photoanode, even as individual nanowires begin degrading (*189*). Efforts have also been made to deposit nanowire photoelectrodes onto flexible substrates (*190*), which are compatible with modern fabrication techniques (*191*). By combining these scalable deposition techniques with the unique control of nanowire synthesis, photochemical diodes may come closer to practical applications under real-world operating conditions.

REFERENCES AND NOTES

1. International Energy Agency, *Key World Energy Statistics* 2019 (2019); https://webstore.iea.org/download/direct/2831?fileName=Key_World_Energy_Statistics_2019.pdf.
2. J. H. Kim, D. Hansora, P. Sharma, J.-W. Jang, J. S. Lee, Toward practical solar hydrogen production—An artificial photosynthetic leaf-to-farm challenge. *Chem. Soc. Rev.* **48**, 1908–1971 (2019).
3. J. W. Choi, D. Aurbach, Promise and reality of post-lithium-ion batteries with high energy densities. *Nat. Rev. Mater.* **1**, 16013 (2016).
4. J.-M. Tarascon, M. Armand, Issues and challenges facing rechargeable lithium batteries. *Nature* **414**, 359–367 (2001).
5. A. J. Nozik, Photochemical diodes. *Appl. Phys. Lett.* **30**, 567–569 (1977).
6. S. Y. Reece, J. A. Hamel, K. Sung, T. D. Jarvi, A. J. Esswein, P. J. H. Pijpers, D. G. Nocera, Wireless solar water splitting using silicon-based semiconductors and earth-abundant catalysts. *Science* **334**, 645–648 (2011).
7. D. G. Nocera, The artificial leaf. *Acc. Chem. Res.* **45**, 767–776 (2012).
8. J. Deng, Y. Su, D. Liu, P. Yang, B. Liu, C. Liu, Nanowire photoelectrochemistry. *Chem. Rev.* **119**, 9221–9259 (2019).
9. A. J. E. Rettie, H. C. Lee, L. G. Marshall, J.-F. Lin, C. Capan, J. Lindemuth, J. S. McCloy, J. Zhou, A. J. Bard, C. B. Mullins, Combined charge carrier transport and photoelectrochemical characterization of $BiVO_4$ single crystals: Intrinsic behavior of a complex metal oxide. *J. Am. Chem. Soc.* **135**, 11389–11396 (2013).
10. A. P. Levitt, *Whisker Technology* (Wiley-Interscience, 1970).
11. R. S. Wagner, W. C. Ellis, Vapor-liquid-solid mechanism of single crystal growth. *Appl. Phys. Lett.* **4**, 89–90 (1964).
12. B. Wu, A. Kumar, S. Pamarthy, High aspect ratio silicon etch: A review. *J. Appl. Phys.* **108**, 51101 (2010).
13. K. Q. Peng, Z. P. Huang, J. Zhu, Fabrication of large-area silicon nanowire p–n junction diode arrays. *Adv. Mater.* **16**, 73–76 (2004).
14. A. M. Morales, C. M. Lieber, A laser ablation method for the synthesis of crystalline semiconductor nanowires. *Science* **279**, 208–211 (1998).
15. N. P. Dasgupta, J. Sun, C. Liu, S. Brittman, S. C. Andrews, J. Lim, H. Gao, R. Yan, P. Yang, 25th anniversary article: Semiconductor nanowires—Synthesis, characterization, and applications. *Adv. Mater.* **26**, 2137–2184 (2014).
16. L. Samuelson, C. Thelander, M. T. Björk, M. Borgström, K. Deppert, K. A. Dick, A. E. Hansen, T. Mårtensson, N. Panev, A. I. Persson, W. Seifert, N. Sköld, M. W. Larsson, L. R. Wallenberg, Semiconductor nanowires for 0D and 1D physics and applications. *Phys. E* **25**, 313–318 (2004).
17. J. Hu, M. Ouyang, P. Yang, C. M. Lieber, Controlled growth and electrical properties of heterojunctions of carbon nanotubes and silicon nanowires. *Nature* **399**, 48–51 (1999).
18. S. Gubbala, V. Chakrapani, V. Kumar, M. K. Sunkara, Band-edge engineered hybrid structures for dye-sensitized solar cells based on SnO_2 nanowires. *Adv. Funct. Mater.* **18**, 2411–2418 (2008).
19. M. Law, L. E. Greene, J. C. Johnson, R. Saykally, P. Yang, Nanowire dye-sensitized solar cells. *Nat. Mater.* **4**, 455–459 (2005).
20. M. Law, L. E. Greene, A. Radenovic, T. Kuykendall, J. Liphardt, P. Yang, ZnO–Al_2O_3 and ZnO–TiO_2 core–shell nanowire dye-sensitized solar cells. *J. Phys. Chem. B* **110**, 22652–22663 (2006).
21. K. S. Leschkies, R. Divakar, J. Basu, E. Enache-Pommer, J. E. Boercker, C. B. Carter, U. R. Kortshagen, D. J. Norris, E. S. Aydil, Photosensitization of ZnO nanowires with CdSe quantum dots for photovoltaic devices. *Nano Lett.* **7**, 1793–1798 (2007).
22. J.-Y. Liao, B.-X. Lei, H.-Y. Chen, D.-B. Kuang, C.-Y. Su, Oriented hierarchical single crystalline anatase TiO_2 nanowire arrays on Ti-foil substrate for efficient flexible dye-sensitized solar cells. *Energy Environ. Sci.* **5**, 5750–5757 (2012).
23. Q. Zhang, G. Cao, Nanostructured photoelectrodes for dye-sensitized solar cells. *Nano Today* **6**, 91–109 (2011).
24. J. Wallentin, N. Anttu, D. Asoli, M. Huffman, I. Åberg, M. H. Magnusson, G. Siefer, P. Fuss-Kailuweit, F. Dimroth, B. Witzigmann, H. Q. Xu, L. Samuelson, K. Deppert, M. T. Borgström, InP nanowire array solar cells achieving 13.8% efficiency by exceeding the ray optics limit. *Science* **339**, 1057–1060 (2013).
25. X. Wang, Q. Wu, H. Ma, C. Ma, Z. Yu, Y. Fu, X. Dong, Fabrication of PbO_2 tipped Co_3O_4 nanowires for efficient photoelectrochemical decolorization of dye (reactive brilliant blue KN-R) wastewater. *Sol. Energy Mater. Sol. Cells* **191**, 381–388 (2019).
26. H. Zhou, X. Sheng, J. Xiao, Z. Ding, D. Wang, X. Zhang, J. Liu, R. Wu, X. Feng, L. Jiang, Increasing the efficiency of photocatalytic reactions via surface microenvironment engineering. *J. Am. Chem. Soc.* **142**, 2738–2743 (2020).
27. C. K. Chan, H. Peng, G. Liu, K. McIlwrath, X. F. Zhang, R. A. Huggins, Y. Cui, High-performance lithium battery anodes using silicon nanowires. *Nat. Nanotechnol.* **3**, 31–35 (2008).
28. L. Mai, X. Tian, X. Xu, L. Chang, L. Xu, Nanowire electrodes for electrochemical energy storage devices. *Chem. Rev.* **114**, 11828–11862 (2014).
29. J. Liu, J. Jiang, C. Cheng, H. Li, J. Zhang, H. Gong, H. J. Fan, Co_3O_4 nanowire@MnO_2 ultrathin nanosheet core/shell arrays: A new class of high-performance pseudocapacitive materials. *Adv. Mater.* **23**, 2076–2081 (2011).
30. X. Lu, M. Yu, G. Wang, T. Zhai, S. Xie, Y. Ling, Y. Tong, Y. Li, H-TiO_2@MnO_2//H-TiO_2@C core–shell nanowires for high performance and flexible asymmetric supercapacitors. *Adv. Mater.* **25**, 267–272 (2013).
31. R. Franking, L. Li, M. A. Lukowski, F. Meng, Y. Tan, R. J. Hamers, S. Jin, Facile post-growth doping of nanostructured hematite photoanodes for enhanced photoelectrochemical water oxidation. *Energy Environ. Sci.* **6**, 500–512 (2013).
32. S. Hu, C.-Y. Chi, K. T. Fountaine, M. Yao, H. A. Atwater, P. D. Dapkus, N. S. Lewis, C. Zhou, Optical, electrical, and solar energy-conversion properties of gallium arsenide nanowire-array photoanodes. *Energy Environ. Sci.* **6**, 1879–1890 (2013).
33. Y. J. Hwang, C. H. Wu, C. Hahn, H. E. Jeong, P. Yang, Si/InGaN core/shell hierarchical nanowire arrays and their photoelectrochemical properties. *Nano Lett.* **12**, 1678–1682 (2012).
34. B. Liu, C.-H. Wu, J. Miao, P. Yang, All inorganic semiconductor nanowire mesh for direct solar water splitting. *ACS Nano* **8**, 11739–11744 (2014).
35. C. Liu, J. Tang, H. M. Chen, B. Liu, P. Yang, A fully integrated nanosystem of semiconductor nanowires for direct solar water splitting. *Nano Lett.* **13**, 2989–2992 (2013).
36. C. Liu, N. P. Dasgupta, P. Yang, Semiconductor nanowires for artificial photosynthesis. *Chem. Mater.* **26**, 415–422 (2014).
37. J. R. McKone, H. B. Gray, N. S. Lewis, B. Brunschwig, E. L. Warren, S. W. Boettcher, M. J. Bierman, Nickel-based electrocatalytic photoelectrodes, U.S. Patent US20120313073A1 (2012).
38. Helios Solar Energy Research Center, *Goals & Challenges*; www2.lbl.gov/LBL-Programs/helios-serc/html/goals.html [accessed on 18 Nov 2022].
39. Y. Wu, H. Yan, P. Yang, Semiconductor nanowire array: Potential substrates for photocatalysis and photovoltaics. *Top. Catal.* **19**, 197–202 (2002).
40. V. Andrei, B. Reuillard, E. Reisner, Bias-free solar syngas production by integrating a molecular cobalt catalyst with perovskite–$BiVO_4$ tandems. *Nat. Mater.* **19**, 189–194 (2020).
41. V. Andrei, R. A. Jagt, M. Rahaman, L. Lari, V. K. Lazarov, J. L. MacManus-Driscoll, R. L. Z. Hoye, E. Reisner, Long-term solar water and CO_2 splitting with photoelectrochemical BiOI–$BiVO_4$ tandems. *Nat. Mater.* **21**, 864–868 (2022).
42. S. P. Bremner, M. Y. Levy, C. B. Honsberg, Analysis of tandem solar cell efficiencies under AM1.5G spectrum using a rapid flux calculation method. *Prog. Photovolt. Res. Appl.* **16**, 225–233 (2008).

43. S. Hu, C. Xiang, S. Haussener, A. D. Berger, N. S. Lewis, An analysis of the optimal band gaps of light absorbers in integrated tandem photoelectrochemical water-splitting systems. *Energy Environ. Sci.* **6**, 2984–2993 (2013).
44. M. Speckbacher, J. Treu, T. J. Whittles, W. M. Linhart, X. Xu, K. Saller, V. R. Dhanak, G. Abstreiter, J. J. Finley, T. D. Veal, G. Koblmüller, Direct measurements of fermi level pinning at the surface of intrinsically N-type InGaAs nanowires. *Nano Lett.* **16**, 5135–5142 (2016).
45. B. H. Simpson, J. Rodríguez-López, Electrochemical imaging and redox interrogation of surface defects on operating $SrTiO_3$ photoelectrodes. *J. Am. Chem. Soc.* **137**, 14865–14868 (2015).
46. B. Seger, T. Pedersen, A. B. Laursen, P. C. K. Vesborg, O. Hansen, I. Chorkendorff, Using TiO_2 as a conductive protective layer for photocathodic H_2 evolution. *J. Am. Chem. Soc.* **135**, 1057–1064 (2013).
47. S. Hu, M. R. Shaner, J. A. Beardslee, M. Lichterman, B. S. Brunschwig, N. S. Lewis, Amorphous TiO_2 coatings stabilize Si, GaAs, and GaP photoanodes for efficient water oxidation. *Science* **344**, 1005–1009 (2014).
48. D. Bae, B. Seger, O. Hansen, P. C. K. Vesborg, I. Chorkendorff, Durability testing of photoelectrochemical hydrogen production under day/night light cycled conditions. *ChemElectroChem* **6**, 106–109 (2019).
49. E. D. Palik, J. W. Faust, H. F. Gray, R. F. Greene, Study of the Etch-stop mechanism in silicon. *J. Electrochem. Soc.* **129**, 2051 (1982).
50. H. Ali-Löytty, M. Hannula, M. Valden, A. Eilert, H. Ogasawara, A. Nilsson, Chemical dissolution of Pt(111) during potential cycling under negative pH conditions studied by operando x-ray photoelectron spectroscopy. *J. Phys. Chem. C* **123**, 25128–25134 (2019).
51. L. Cai, J. Zhao, H. Li, J. Park, I. S. Cho, H. S. Han, X. Zheng, One-step hydrothermal deposition of Ni:FeOOH onto photoanodes for enhanced water oxidation. *ACS Energy Lett.* **1**, 624–632 (2016).
52. A. J. Bard, Photoelectrochemistry and heterogeneous photo-catalysis at semiconductors. *J. Photochem.* **10**, 59–75 (1979).
53. J. M. Foley, M. J. Price, J. I. Feldblyum, S. Maldonado, Analysis of the operation of thin nanowire photoelectrodes for solar energy conversion. *Energy Environ. Sci.* **5**, 5203–5220 (2012).
54. A. Fitch, N. C. Strandwitz, B. S. Brunschwig, N. S. Lewis, A comparison of the behavior of single crystalline and nanowire array ZnO photoanodes. *J. Phys. Chem. C* **117**, 2008–2015 (2013).
55. E. L. Warren, S. W. Boettcher, M. G. Walter, H. A. Atwater, N. S. Lewis, pH-independent, 520 mV open-circuit voltages of Si/methyl viologen$^{2+/+}$ contacts through use of radial n^+p-Si junction microwire array photoelectrodes. *J. Phys. Chem. C* **115**, 594–598 (2011).
56. C. Liu, J. Sun, J. Tang, P. Yang, Zn-doped p-type gallium phosphide nanowire photocathodes from a surfactant-free solution synthesis. *Nano Lett.* **12**, 5407–5411 (2012).
57. Y. W. Chen, J. D. Prange, S. Dühnen, Y. Park, M. Gunji, C. E. D. Chidsey, P. C. McIntyre, Atomic layer-deposited tunnel oxide stabilizes silicon photoanodes for water oxidation. *Nat. Mater.* **10**, 539–544 (2011).
58. Y. Wan, S. K. Karuturi, C. Samundsett, J. Bullock, M. Hettick, D. Yan, J. Peng, P. R. Narangari, S. Mokkapati, H. H. Tan, C. Jagadish, A. Javey, A. Cuevas, Tantalum oxide electron-selective heterocontacts for silicon photovoltaics and photoelectrochemical water reduction. *ACS Energy Lett.* **3**, 125–131 (2018).
59. P. A. Kohl, S. N. Frank, A. J. Bard, Semiconductor electrodes: XI. Behavior of n- and p-type single crystal semconductors covered with thin n-TiO_2 films. *J. Electrochem. Soc.* **124**, 225–229 (1977).
60. C. F. Jewell, A. Subramanian, C.-Y. Nam, R. G. Finke, Ultrathin alumina passivation for improved photoelectrochemical water oxidation catalysis of tin oxide sensitized by a phosphonate-functionalized perylene diimide first without, and then with, CoO_y. *Sustain. Energy Fuels* **5**, 5257–5269 (2021).
61. G. Liu, P. R. Narangari, Q. T. Trinh, W. Tu, M. Kraft, H. H. Tan, C. Jagadish, T. S. Choksi, J. W. Ager, S. Karuturi, R. Xu, Manipulating intermediates at the Au–TiO_2 interface over InP nanopillar array for photoelectrochemical CO_2 reduction. *ACS Catal.* **11**, 11416–11428 (2021).
62. Y. Hori, H. Wakebe, T. Tsukamoto, O. Koga, Electrocatalytic process of CO selectivity in electrochemical reduction of CO_2 at metal electrodes in aqueous media. *Electrochim. Acta* **39**, 1833–1839 (1994).
63. L. Hu, G. Chen, Analysis of optical absorption in silicon nanowire arrays for photovoltaic applications. *Nano Lett.* **7**, 3249–3252 (2007).
64. R. A. Street, P. Qi, R. Lujan, W. S. Wong, Reflectivity of disordered silicon nanowires. *Appl. Phys. Lett.* **93**, 163109 (2008).
65. J. Li, H. Yu, Y. Li, Solar energy harnessing in hexagonally arranged Si nanowire arrays and effects of array symmetry on optical characteristics. *Nanotechnol.* **23**, 194010 (2012).
66. J. Li, H. Yu, S. M. Wong, G. Zhang, X. Sun, P. G.-Q. Lo, D.-L. Kwong, Si nanopillar array optimization on Si thin films for solar energy harvesting. *Appl. Phys. Lett.* **95**, 33102 (2009).
67. S. W. Boettcher, E. L. Warren, M. C. Putnam, E. A. Santori, D. Turner-Evans, M. D. Kelzenberg, M. G. Walter, J. R. McKone, B. S. Brunschwig, H. A. Atwater, N. S. Lewis, Photoelectrochemical hydrogen evolution using Si microwire arrays. *J. Am. Chem. Soc.* **133**, 1216–1219 (2011).
68. L. Liu, F. Lu, J. Tian, X. Zhangyang, Enhancement of electron collection and light trapping of inclined GaN and AlGaN nanowire arrays. *Energy Technol.* **9**, 2000801 (2021).
69. P. A. Kempler, M. H. Richter, W.-H. Cheng, B. S. Brunschwig, N. S. Lewis, Si microwire-array photocathodes decorated with Cu allow CO_2 reduction with minimal parasitic absorption of sunlight. *ACS Energy Lett.* **5**, 2528–2534 (2020).
70. A. Fujishima, K. Honda, Electrochemical photolysis of water at a semiconductor electrode. *Nature* **238**, 37–38 (1972).
71. Q. Kong, D. Kim, C. Liu, Y. Yu, Y. Su, Y. Li, P. Yang, Directed assembly of nanoparticle catalysts on nanowire photoelectrodes for photoelectrochemical CO_2 reduction. *Nano Lett.* **16**, 5675–5680 (2016).
72. C. Liu, J. J. Gallagher, K. K. Sakimoto, E. M. Nichols, C. J. Chang, M. C. Y. Chang, P. Yang, Nanowire–bacteria hybrids for unassisted solar carbon dioxide fixation to value-added chemicals. *Nano Lett.* **15**, 3634–3639 (2015).
73. N. Kornienko, J. Z. Zhang, K. K. Sakimoto, P. Yang, E. Reisner, Interfacing nature's catalytic machinery with synthetic materials for semi-artificial photosynthesis. *Nat. Nanotechnol.* **13**, 890–899 (2018).
74. H. Zhou, M. Feng, M. Feng, X. Gong, D. Zhang, Y. Zhou, S. Chen, Gradient doping of sulfur in Sb_2Se_3 nanowire arrays as photoelectrochemical photocathode with a 2% half-cell solar-to-hydrogen conversion efficiency. *Appl. Phys. Lett.* **116**, 113902 (2020).
75. N. P. Dasgupta, C. Liu, S. Andrews, F. B. Prinz, P. Yang, Atomic layer deposition of platinum catalysts on nanowire surfaces for photoelectrochemical water reduction. *J. Am. Chem. Soc.* **135**, 12932–12935 (2013).
76. S. Vanka, K. Sun, G. Zeng, T. A. Pham, F. M. Toma, T. Ogitsu, Z. Mi, Long-term stability studies of a semiconductor photoelectrode in three-electrode configuration. *J. Mater. Chem. A* **7**, 27612–27619 (2019).
77. L. Pan, J. H. Kim, M. T. Mayer, M.-K. Son, A. Ummadisingu, J. S. Lee, A. Hagfeldt, J. Luo, M. Grätzel, Boosting the performance of Cu_2O photocathodes for unassisted solar water splitting devices. *Nat. Catal.* **1**, 412–420 (2018).
78. L. Pan, Y. Liu, L. Yao, D. Ren, K. Sivula, M. Grätzel, A. Hagfeldt, Cu_2O photocathodes with band-tail states assisted hole transport for standalone solar water splitting. *Nat. Commun.* **11**, 318 (2020).
79. I. Oh, J. Kye, S. Hwang, Enhanced photoelectrochemical hydrogen production from silicon nanowire array photocathode. *Nano Lett.* **12**, 298–302 (2012).
80. L. Zhang, C. Liu, A. B. Wong, J. Resasco, P. Yang, MoS_2-wrapped silicon nanowires for photoelectrochemical water reduction. *Nano Res.* **8**, 281–287 (2015).
81. D. Hu, J. Xiang, Q. Zhou, S. Su, Z. Zhang, X. Wang, M. Jin, L. Nian, R. Nözel, G. Zhou, Z. Zhang, J. Liu, One-step chemical vapor deposition of MoS_2 nanosheets on SiNWs as photocathodes for efficient and stable solar-driven hydrogen production. *Nanoscale* **10**, 3518–3525 (2018).
82. Z. Huang, Z. Chen, Z. Chen, C. Lv, H. Meng, C. Zhang, $Ni_{12}P_5$ nanoparticles as an efficient catalyst for hydrogen generation via electrolysis and photoelectrolysis. *ACS Nano* **8**, 8121–8129 (2014).
83. S. Lee, S. Cha, Y. Myung, K. Park, I. H. Kwak, I. S. Kwon, J. Seo, S. A. Lim, E. H. Cha, J. Park, Orthorhombic $NiSe_2$ nanocrystals on Si nanowires for efficient photoelectrochemical water splitting. *ACS Appl. Mater. Interfaces* **10**, 33198–33204 (2018).
84. S. M. Thalluri, J. Borme, K. Yu, J. Xu, I. Amorim, J. Gaspar, L. Qiao, P. Ferreira, P. Alpuim, L. Liu, Conformal and continuous deposition of bifunctional cobalt phosphide layers on p-silicon nanowire arrays for improved solar hydrogen evolution. *Nano Res.* **11**, 4823–4835 (2018).
85. I. Roger, M. A. Shipman, M. D. Symes, Earth-abundant catalysts for electrochemical and photoelectrochemical water splitting. *Nat. Rev. Chem.* **1**, 3 (2017).
86. A. P. Goodey, S. M. Eichfeld, K.-K. Lew, J. M. Redwing, T. E. Mallouk, Silicon nanowire array photoelectrochemical cells. *J. Am. Chem. Soc.* **129**, 12344–12345 (2007).
87. K.-Q. Peng, X. Wang, X.-L. Wu, S.-T. Lee, Platinum nanoparticle decorated silicon nanowires for efficient solar energy conversion. *Nano Lett.* **9**, 3704–3709 (2009).
88. P. Gnanasekar, D. Periyanagounder, P. Varadhan, J.-H. He, J. Kulandaivel, Highly efficient and stable photoelectrochemical hydrogen evolution with 2D-NbS_2/Si nanowire heterojunction. *ACS Appl. Mater. Interfaces* **11**, 44179–44185 (2019).
89. S. M. Thalluri, J. Borme, D. Xiong, J. Xu, W. Li, I. Amorim, P. Alpuim, J. Gaspar, H. Fonseca, L. Qiao, L. Liu, Highly-ordered silicon nanowire arrays for photoelectrochemical hydrogen evolution: An investigation on the effect of wire diameter, length and inter-wire spacing. *Sustain. Energy Fuels* **2**, 978–982 (2018).
90. Y. Su, C. Liu, S. Brittman, J. Tang, A. Fu, N. Kornienko, Q. Kong, P. Yang, Single-nanowire photoelectrochemistry. *Nat. Nanotechnol.* **11**, 609–612 (2016).

91. B. Zhou, X. Kong, S. Vanka, S. Chu, P. Ghamari, Y. Wang, N. Pant, I. Shih, H. Guo, Z. Mi, Gallium nitride nanowire as a linker of molybdenum sulfides and silicon for photoelectrocatalytic water splitting. *Nat. Commun.* **9**, 3856 (2018).
92. P. Varadhan, H.-C. Fu, D. Priante, J. R. D. Retamal, C. Zhao, M. Ebaid, T. K. Ng, I. Ajia, S. Mitra, I. S. Roqan, B. S. Ooi, J.-H. He, Surface passivation of GaN nanowires for enhanced photoelectrochemical water-splitting. *Nano Lett.* **17**, 1520–1528 (2017).
93. F. Cui, Y. Zhang, H. A. Fonseka, P. Promdet, A. I. Channa, M. Wang, X. Xia, S. Sathasivam, H. Liu, I. P. Parkin, H. Yang, T. Li, K.-L. Choy, J. Wu, C. Blackman, A. M. Sanchez, H. Liu, Robust protection of III–V nanowires in water splitting by a thin compact TiO_2 layer. *ACS Appl. Mater. Interfaces* **13**, 30950–30958 (2021).
94. N. Kornienko, N. A. Gibson, H. Zhang, S. W. Eaton, Y. Yu, S. Aloni, S. R. Leone, P. Yang, Growth and photoelectrochemical energy conversion of Wurtzite Indium phosphide nanowire arrays. *ACS Nano* **10**, 5525–5535 (2016).
95. P. R. Narangari, J. D. Butson, H. H. Tan, C. Jagadish, S. Karuturi, Surface-tailored InP nanowires via self-assembled Au nanodots for efficient and stable photoelectrochemical hydrogen evolution. *Nano Lett.* **21**, 6967–6974 (2021).
96. S. Choi, J. Hwang, T. H. Lee, H.-H. Kim, S.-P. Hong, C. Kim, M.-J. Choi, H. K. Park, S. S. M. Bhat, J. M. Suh, J. Lee, K. S. Choi, S.-H. Hong, J. C. Shin, H. W. Jang, Photoelectrochemical hydrogen production at neutral pH phosphate buffer solution using TiO_2 passivated InAs nanowire/p-Si heterostructure photocathode. *Chem. Eng. J.* **392**, 123688 (2020).
97. J. Luo, L. Steier, M.-K. Son, M. Schreier, M. T. Mayer, M. Grätzel, Cu_2O nanowire photocathodes for efficient and durable solar water splitting. *Nano Lett.* **16**, 1848–1857 (2016).
98. Y. Cao, D. Liu, X. Ni, X. Meng, Y. Zhou, Z. Sun, Y. Kuang, Better charge separation in CuO nanowire array photocathodes: Micro-/nanostructure regulation for photoelectrochemical reaction. *ACS Appl. Energy Mater.* **3**, 6334–6343 (2020).
99. S.-F. Duan, Z.-X. Zhang, Y.-Y. Geng, X.-Q. Yao, M. Kan, Y.-X. Zhao, X.-B. Pan, X.-W. Kang, C.-L. Tao, D.-D. Qin, Brand new 1D branched CuO nanowire arrays for efficient photoelectrochemical water reduction. *Dalton Trans.* **47**, 14566–14572 (2018).
100. A. Kargar, Y. Jing, S. J. Kim, C. T. Riley, X. Pan, D. Wang, ZnO/CuO heterojunction branched nanowires for photoelectrochemical hydrogen generation. *ACS Nano* **7**, 11112–11120 (2013).
101. C.-Y. Lin, Y.-H. Lai, D. Mersch, E. Reisner, $Cu_2O|NiO_x$ nanocomposite as an inexpensive photocathode in photoelectrochemical water splitting. *Chem. Sci.* **3**, 3482–3487 (2012).
102. M. B. Ross, P. de Luna, Y. Li, C.-T. Dinh, D. Kim, P. Yang, E. H. Sargent, Designing materials for electrochemical carbon dioxide recycling. *Nat. Catal.* **2**, 648–658 (2019).
103. D. Ren, J. Fong, B. S. Yeo, The effects of currents and potentials on the selectivities of copper toward carbon dioxide electroreduction. *Nat. Commun.* **9**, 925 (2018).
104. W. J. Dong, J. W. Lim, D. M. Hong, J. Kim, J. Y. Park, W. S. Cho, S. Baek, J.-L. Lee, Grain boundary engineering of Cu–Ag thin-film catalysts for selective (photo)electrochemical CO_2 reduction to CO and CH_4. *ACS Appl. Mater. Interfaces* **13**, 18905–18913 (2021).
105. J. T. Song, H. Ryoo, M. Cho, J. Kim, J.-G. Kim, S.-Y. Chung, J. Oh, Nanoporous Au thin films on Si photoelectrodes for selective and efficient photoelectrochemical CO_2 reduction. *Adv. Energy Mater.* **7**, 1601103 (2017).
106. W.-H. Cheng, M. H. Richter, R. Müller, M. Kelzenberg, S. Yalamanchili, P. R. Jahelka, A. N. Perry, P. C. Wu, R. Saive, F. Dimroth, B. S. Brunschwig, T. Hannappel, H. A. Atwater, Integrated solar-driven device with a front surface semitransparent catalysts for unassisted CO_2 reduction. *Adv. Energy Mater.* **12**, 2201062 (2022).
107. S. Yalamanchili, E. Verlage, W.-H. Cheng, K. T. Fountaine, P. R. Jahelka, P. A. Kempler, R. Saive, N. S. Lewis, H. A. Atwater, High broadband light transmission for solar fuels production using dielectric optical waveguides in TiO_2 nanocone arrays. *Nano Lett.* **20**, 502–508 (2020).
108. K. D. Yang, Y. Ha, U. Sim, J. An, C. W. Lee, K. Jin, Y. Kim, J. Park, J. S. Hong, J. H. Lee, H.-E. Lee, H.-Y. Jeong, H. Kim, K. T. Nam, Graphene quantum sheet catalyzed silicon photocathode for selective CO_2 conversion to CO. *Adv. Funct. Mater.* **26**, 233–242 (2016).
109. S. K. Choi, U. Kang, S. Lee, D. J. Ham, S. M. Ji, H. Park, Sn-coupled p-Si nanowire arrays for solar formate production from CO_2. *Adv. Energy Mater.* **4**, 1301614 (2014).
110. B. A. Zhang, T. Ozel, J. S. Elias, C. Costentin, D. G. Nocera, Interplay of homogeneous reactions, mass transport, and kinetics in determining selectivity of the reduction of CO_2 on gold electrodes. *ACS Cent. Sci.* **5**, 1097–1105 (2019).
111. I. Roh, S. Yu, C.-K. Lin, S. Louisia, S. Cestellos-Blanco, P. Yang, Photoelectrochemical CO_2 reduction toward multicarbon products with silicon nanowire photocathodes interfaced with copper nanoparticles. *J. Am. Chem. Soc.* **144**, 8002–8006 (2022).
112. R. Hinogami, T. Mori, S. Yae, Y. Nakato, Efficient photoelectrochemical reduction of carbon dioxide on a p-type silicon (p-Si) electrode modified with very small copper particles. *Chem. Lett.* **23**, 1725–1728 (1994).
113. Y. Zhang, D. Pan, Y. Tao, H. Shang, D. Zhang, G. Li, H. Li, Photoelectrocatalytic reduction of CO_2 to Syngas via SnO_x-enhanced Cu_2O nanowires photocathodes. *Adv. Funct. Mater.* **32**, 2109600 (2022).
114. R. Liu, C. Stephani, J. J. Han, K. L. Tan, D. Wang, Silicon nanowires show improved performance as photocathode for catalyzed carbon dioxide photofixation. *Angew. Chem. Int. Ed.* **52**, 4225–4228 (2013).
115. K. K. Sakimoto, A. B. Wong, P. Yang, Self-photosensitization of nonphotosynthetic bacteria for solar-to-chemical production. *Science* **351**, 74–77 (2016).
116. S. Xiao, Z. Li, Q. Fu, Y. Li, J. Li, L. Zhang, Q. Liao, X. Zhu, Hybrid microbial photoelectrochemical system reduces CO_2 to CH_4 with 1.28% solar energy conversion efficiency. *Chem. Eng. J.* **390**, 124530 (2020).
117. H. E. Jeong, I. Kim, P. Karam, H.-J. Choi, P. Yang, Bacterial recognition of silicon nanowire arrays. *Nano Lett.* **13**, 2864–2869 (2013).
118. X. Shi, I. Y. Choi, K. Zhang, J. Kwon, D. Y. Kim, J. K. Lee, S. H. Oh, J. K. Kim, J. H. Park, Efficient photoelectrochemical hydrogen production from bismuth vanadate-decorated tungsten trioxide helix nanostructures. *Nat. Commun.* **5**, 4775 (2014).
119. Y. J. Hwang, C. Hahn, B. Liu, P. Yang, Photoelectrochemical properties of TiO_2 nanowire arrays: A study of the dependence on length and atomic layer deposition coating. *ACS Nano* **6**, 5060–5069 (2012).
120. J. Su, X. Feng, J. D. Sloppy, L. Guo, C. A. Grimes, Vertically aligned WO_3 nanowire arrays grown directly on transparent conducting oxide coated glass: Synthesis and photoelectrochemical properties. *Nano Lett.* **11**, 203–208 (2011).
121. T. W. Kim, K.-S. Choi, Nanoporous $BiVO_4$ photoanodes with dual-layer oxygen evolution catalysts for solar water splitting. *Science* **343**, 990–994 (2014).
122. Y. Ling, G. Wang, D. A. Wheeler, J. Z. Zhang, Y. Li, Sn-doped hematite nanostructures for photoelectrochemical water splitting. *Nano Lett.* **11**, 2119–2125 (2011).
123. D. A. Grave, D. S. Ellis, Y. Piekner, M. Kölbach, H. Dotan, A. Kay, P. Schnell, R. van de Krol, F. F. Abdi, D. Friedrich, A. Rothschild, Extraction of mobile charge carrier photogeneration yield spectrum of ultrathin-film metal oxide photoanodes for solar water splitting. *Nat. Mater.* **20**, 1579 (2021).
124. S. S. Kalanur, Y. J. Hwang, S. Y. Chae, O. S. Joo, Facile growth of aligned WO_3 nanorods on FTO substrate for enhanced photoanodic water oxidation activity. *J. Mater. Chem. A* **1**, 3479–3488 (2013).
125. L. Li, Y. Yu, F. Meng, Y. Tan, R. J. Hamers, S. Jin, Facile solution synthesis of α-$FeF_3{\cdot}3H_2O$ nanowires and their conversion to α-Fe_2O_3 nanowires for photoelectrochemical application. *Nano Lett.* **12**, 724–731 (2012).
126. J. Wang, M. Wang, T. Zhang, Z. Wang, P. Guo, J. Su, L. Guo, Facile synthesis of ultrafine hematite nanowire arrays in mixed water–ethanol–acetic acid solution for enhanced charge transport and separation. *ACS Appl. Mater. Interfaces* **10**, 12594–12602 (2018).
127. P. Quitério, A. Apolinário, D. Navas, S. Magalhães, E. Alves, A. Mendes, C. T. Sousa, J. P. Araújo, Photoelectrochemical water splitting: Thermal annealing challenges on hematite nanowires. *J. Phys. Chem. C* **124**, 12897–12911 (2020).
128. X. Song, W. Li, D. He, H. Wu, Z. Ke, C. Jiang, G. Wang, X. Xiao, The "Midas Touch" transformation of TiO_2 nanowire arrays during visible light photoelectrochemical performance by carbon/nitrogen coimplantation. *Adv. Energy Mater.* **8**, 1800165 (2018).
129. S. Hoang, S. Guo, N. T. Hahn, A. J. Bard, C. B. Mullins, Visible light driven photoelectrochemical water oxidation on nitrogen-modified TiO_2 nanowires. *Nano Lett.* **12**, 26–32 (2012).
130. X. Yang, A. Wolcott, G. Wang, A. Sobo, R. C. Fitzmorris, F. Qian, J. Z. Zhang, Y. Li, Nitrogen-doped ZnO nanowire arrays for photoelectrochemical water splitting. *Nano Lett.* **9**, 2331–2336 (2009).
131. M. Xu, P. Da, H. Wu, D. Zhao, G. Zheng, Controlled Sn-doping in TiO_2 nanowire photoanodes with enhanced photoelectrochemical conversion. *Nano Lett.* **12**, 1503–1508 (2012).
132. G. Wang, H. Wang, Y. Ling, Y. Tang, X. Yang, R. C. Fitzmorris, C. Wang, J. Z. Zhang, Y. Li, Hydrogen-treated TiO_2 nanowire arrays for photoelectrochemical water splitting. *Nano Lett.* **11**, 3026–3033 (2011).
133. S. Hoang, S. P. Berglund, N. T. Hahn, A. J. Bard, C. B. Mullins, Enhancing visible light photooxidation of water with TiO_2 nanowire arrays via cotreatment with H_2 and NH_3: Synergistic effects between Ti^{3+} and N. *J. Am. Chem. Soc.* **134**, 3659–3662 (2012).
134. M. Li, Y. Yang, Y. Ling, W. Qiu, F. Wang, T. Liu, Y. Song, X. Liu, P. Fang, Y. Tong, Y. Li, Morphology and doping engineering of Sn-doped hematite nanowire photoanodes. *Nano Lett.* **17**, 2490–2495 (2017).
135. Y. Ling, G. Wang, J. Reddy, C. Wang, J. Z. Zhang, Y. Li, The influence of oxygen content on the thermal activation of hematite nanowires. *Angew. Chem. Int. Ed.* **51**, 4074–4079 (2012).
136. M. Shao, F. Ning, M. Wei, D. G. Evans, X. Duan, Hierarchical nanowire arrays based on ZnO core–layered double hydroxide shell for largely enhanced photoelectrochemical water splitting. *Adv. Funct. Mater.* **24**, 580–586 (2014).
137. A. Ghobadi, T. G. U. Ghobadi, F. Karadas, E. Ozbay, Angstrom thick ZnO passivation layer to improve the photoelectrochemical water splitting performance of a TiO_2 nanowire photoanode: The role of deposition temperature. *Sci. Rep.* **8**, 16322 (2018).

138. F. Wu, Y. Yu, H. Yang, L. N. German, Z. Li, J. Chen, W. Yang, L. Huang, W. Shi, L. Wang, X. Wang, Simultaneous enhancement of charge separation and hole transportation in a TiO_2–$SrTiO_3$ core–shell nanowire photoelectrochemical system. *Adv. Mater.* **29**, 1701432 (2017).
139. A. R. Bielinski, A. J. Gayle, S. Lee, N. P. Dasgupta, Geometric optimization of bismuth vanadate core–shell nanowire photoanodes using atomic layer deposition. *ACS Appl. Mater. Interfaces* **13**, 52063–52072 (2021).
140. P. M. Rao, L. Cai, C. Liu, I. S. Cho, C. H. Lee, J. M. Weisse, P. Yang, X. Zheng, Simultaneously efficient light absorption and charge separation in WO_3/$BiVO_4$ core/shell nanowire photoanode for photoelectrochemical water oxidation. *Nano Lett.* **14**, 1099–1105 (2014).
141. Y. Chen, L. Wang, W. Wang, M. Cao, Enhanced photoelectrochemical properties of ZnO/ZnSe/CdSe/Cu_{2-x}Se core–shell nanowire arrays fabricated by ion-replacement method. *Appl. Catal. B Environ.* **209**, 110–117 (2017).
142. M. T. Mayer, C. Du, D. Wang, Hematite/Si nanowire dual-absorber system for photoelectrochemical water splitting at low applied potentials. *J. Am. Chem. Soc.* **134**, 12406–12409 (2012).
143. J. Shi, Y. Hara, C. Sun, M. A. Anderson, X. Wang, Three-dimensional high-density hierarchical nanowire architecture for high-performance photoelectrochemical electrodes. *Nano Lett.* **11**, 3413–3419 (2011).
144. M. A. Hassan, A. Waseem, M. A. Johar, I. V. Bagal, J.-S. Ha, S.-W. Ryu, Single-step fabrication of 3D hierarchical ZnO/ZnS heterojunction branched nanowires by MOCVD for enhanced photoelectrochemical water splitting. *J. Mater. Chem. A* **8**, 8300–8312 (2020).
145. G. Ai, H. Li, S. Liu, R. Mo, J. Zhong, Solar water splitting by TiO_2/CdS/Co–Pi nanowire array photoanode enhanced with Co–Pi as hole transfer relay and CdS as light absorber. *Adv. Funct. Mater.* **25**, 5706–5713 (2015).
146. H. M. Chen, C. K. Chen, Y.-C. Chang, C.-W. Tsai, R.-S. Liu, S.-F. Hu, W.-S. Chang, K.-H. Chen, Quantum dot monolayer sensitized ZnO nanowire-array photoelectrodes: True efficiency for water splitting. *Angew. Chem. Int. Ed.* **49**, 5966–5969 (2010).
147. G. Wang, X. Yang, F. Qian, J. Z. Zhang, Y. Li, Double-sided CdS and CdSe quantum dot cosensitized ZnO nanowire arrays for photoelectrochemical hydrogen generation. *Nano Lett.* **10**, 1088–1092 (2010).
148. J. Hensel, G. Wang, Y. Li, J. Z. Zhang, Synergistic effect of CdSe quantum dot sensitization and nitrogen doping of TiO_2 nanostructures for photoelectrochemical solar hydrogen generation. *Nano Lett.* **10**, 478–483 (2010).
149. N. Chen, Y. Hu, X. Liu, J. Yang, W. Li, D. Lu, J. Fu, Y. Liang, W. Wang, A dual-heterojunction Cu_2O/CdS/ZnO nanotube array photoanode for highly efficient photoelectrochemical solar-driven hydrogen production with 2.8% efficiency. *J. Phys. Chem. C* **124**, 21968–21977 (2020).
150. K. Jiang, W. Wang, J. Wang, T. Zhu, L. Yao, Y. Cheng, Y. Wang, Y. Liang, J. Fu, Cu_2O nanoparticles sensitize TiO_2/CdS nanowire arrays to prolong charge carrier lifetime and highly enhance unassisted photoelectrochemical hydrogen generation with 4.3% efficiency. *Dalton Trans.* **49**, 9282–9293 (2020).
151. X. Zhang, Y. Liu, Z. Kang, 3D branched ZnO nanowire arrays decorated with plasmonic Au nanoparticles for high-performance photoelectrochemical water splitting. *ACS Appl. Mater. Interfaces* **6**, 4480–4489 (2014).
152. Y.-C. Pu, G. Wang, K.-D. Chang, Y. Ling, Y.-K. Lin, B. C. Fitzmorris, C.-M. Liu, X. Lu, Y. Tong, J. Z. Zhang, Y.-J. Hsu, Y. Li, Au nanostructure-decorated tio_2 nanowires exhibiting photoactivity across entire UV-visible region for photoelectrochemical water splitting. *Nano Lett.* **13**, 3817–3823 (2013).
153. Z. W. Seh, J. Kibsgaard, C. F. Dickens, I. Chorkendorff, J. K. Nørskov, T. F. Jaramillo, Combining theory and experiment in electrocatalysis: Insights into materials design. *Science* **355**, eaad4998 (2017).
154. S. Chu, S. Vanka, Y. Wang, J. Gim, Y. Wang, Y.-H. Ra, R. Hovden, H. Guo, I. Shih, Z. Mi, Solar water oxidation by an InGaN nanowire photoanode with a Bandgap of 1.7 eV. *ACS Energy Lett.* **3**, 307–314 (2018).
155. Q. Wang, S. Okunaka, H. Tokudome, T. Hisatomi, M. Nakabayashi, N. Shibata, T. Yamada, K. Domen, Printable photocatalyst sheets incorporating a transparent conductive mediator for Z-scheme water splitting. *Joule* **2**, 2667–2680 (2018).
156. P. Xu, J. Feng, T. Fang, X. Zhao, Z. Li, Z. Zou, Photoelectrochemical cell for unassisted overall solar water splitting using a $BiVO_4$ photoanode and Si nanoarray photocathode. *RSC Adv.* **6**, 9905–9910 (2016).
157. V. Andrei, G. M. Ucoski, C. Pornrungroj, C. Uswachoke, Q. Wang, D. S. Achilleos, H. Kasap, K. P. Sokol, R. A. Jagt, H. Lu, T. Lawson, A. Wagner, S. D. Pike, D. S. Wright, R. L. Z. Hoye, J. L. MacManus-Driscoll, H. J. Joyce, R. H. Friend, E. Reisner, Floating perovskite-$BiVO_4$ devices for scalable solar fuel production. *Nature* **608**, 518–522 (2022).
158. D. Gogoi, A. K. Shah, P. Rambabu, M. Qureshi, A. K. Golder, N. R. Peela, Step-scheme heterojunction between CdS nanowires and facet-selective assembly of MnO_x-$BiVO_4$ for an efficient visible-light-driven overall water splitting. *ACS Appl. Mater. Interfaces* **13**, 45475–45487 (2021).
159. M. G. Kibria, F. A. Chowdhury, S. Zhao, B. AlOtaibi, M. L. Trudeau, H. Guo, Z. Mi, Visible light-driven efficient overall water splitting using p-type metal-nitride nanowire arrays. *Nat. Commun.* **6**, 6797 (2015).
160. S. Nitopi, E. Bertheussen, S. B. Scott, X. Liu, A. K. Engstfeld, S. Horch, B. Seger, I. E. L. Stephens, K. Chan, C. Hahn, J. K. Nørskov, T. F. Jaramillo, I. Chorkendorff, Progress and perspectives of electrochemical co_2 reduction on copper in aqueous electrolyte. *Chem. Rev.* **119**, 7610–7672 (2019).
161. Y. Su, S. Cestellos-Blanco, J. M. Kim, Y.-X. Shen, Q. Kong, D. Lu, C. Liu, H. Zhang, Y. Cao, P. Yang, Close-packed nanowire-bacteria hybrids for efficient solar-driven CO_2 fixation. *Joule* **4**, 800–811 (2020).
162. S. Haussener, C. Xiang, J. M. Spurgeon, S. Ardo, N. S. Lewis, A. Z. Weber, Modeling, simulation, and design criteria for photoelectrochemical water-splitting systems. *Energy Environ. Sci.* **5**, 9922–9935 (2012).
163. M. A. Modestino, K. A. Walczak, A. Berger, C. M. Evans, S. Haussener, C. Koval, J. S. Newman, J. W. Ager, R. A. Segalman, Robust production of purified H_2 in a stable, self-regulating, and continuously operating solar fuel generator. *Energy Environ. Sci.* **7**, 297–301 (2014).
164. H. Nishiyama, T. Yamada, M. Nakabayashi, Y. Maehara, M. Yamaguchi, Y. Kuromiya, H. Tokudome, S. Akiyama, T. Watanabe, R. Narushima, S. Okunaka, N. Shibata, T. Takata, T. Hisatomi, K. Domen, Photocatalytic solar hydrogen production from water on a 100 m^2-scale. *Nature* **598**, 304–307 (2021).
165. D. He, T. Jin, W. Li, S. Pantovich, D. Wang, G. Li, Photoelectrochemical co_2 reduction by a molecular cobalt(II) catalyst on planar and nanostructured Si surfaces. *Chem. Eur. J.* **22**, 13064–13067 (2016).
166. P. M. Kraus, M. Zürch, S. K. Cushing, D. M. Neumark, S. R. Leone, The ultrafast X-ray spectroscopic revolution in chemical dynamics. *Nat. Rev. Chem.* **2**, 82–94 (2018).
167. D. K. Schroder, Carrier lifetimes in silicon. *IEEE Trans. Electron Devices* **44**, 160–170 (1997).
168. M. E. Orazem, B. Tribollet, A tutorial on electrochemical impedance spectroscopy. *ChemTexts* **6**, 12 (2020).
169. J. Kretzschmar, F. Harnisch, Electrochemical impedance spectroscopy on biofilm electrodes—Conclusive or euphonious? *Curr. Opin. Electrochem.* **29**, 100757 (2021).
170. H. Wang, S. B. Naghadeh, C. Li, V. L. Cherrette, P. Fang, K. Xu, J. Z. Zhang, Enhanced photoelectrochemical and photocatalytic properties of CdS nanowires decorated with Ni_3S_2 nanoparticles under visible light irradiation. *J. Electrochem. Soc.* **166**, H3146 (2019).
171. Y. Wang, Y.-Y. Zhang, J. Tang, H. Wu, M. Xu, Z. Peng, X.-G. Gong, G. Zheng, Simultaneous etching and doping of TiO_2 nanowire arrays for enhanced photoelectrochemical performance. *ACS Nano* **7**, 9375–9383 (2013).
172. H. Liu, I. M. Klein, J. M. Michelsen, S. K. Cushing, Element-specific electronic and structural dynamics using transient XUV and soft X-ray spectroscopy. *Chem* **7**, 2569–2584 (2021).
173. S. K. Cushing, I. J. Porter, B. R. de Roulet, A. Lee, B. M. Marsh, S. Szoke, M. E. Vaida, S. R. Leone, Layer-resolved ultrafast extreme ultraviolet measurement of hole transport in a Ni-TiO_2-Si photoanode. *Sci. Adv.* **6**, eaay6650 (2022).
174. T. Tachikawa, T. Majima, Exploring the spatial distribution and transport behavior of charge carriers in a single titania nanowire. *J. Am. Chem. Soc.* **131**, 8485–8495 (2009).
175. C. Liu, Y. J. Hwang, H. E. Jeong, P. Yang, Light-induced charge transport within a single asymmetric nanowire. *Nano Lett.* **11**, 3755–3758 (2011).
176. S. Y. Yang, J. Seidel, S. J. Byrnes, P. Shafer, C.-H. Yang, M. D. Rossell, P. Yu, Y.-H. Chu, J. F. Scott, J. W. Ager, L. W. Martin, R. Ramesh, Above-bandgap voltages from ferroelectric photovoltaic devices. *Nat. Nanotechnol.* **5**, 143–147 (2010).
177. Y. Zhang, E. Parsonnet, A. Fernandez, S. M. Griffin, H. Huyan, C.-K. Lin, T. Lei, J. Jin, E. S. Barnard, A. Raja, P. Behera, X. Pan, R. Ramesh, P. Yang, Ferroelectricity in a semiconducting all-inorganic halide perovskite. *Sci. Adv.* **8**, eabj5881 (2022).
178. W. Yang, Y. Yu, M. B. Starr, X. Yin, Z. Li, A. Kvit, S. Wang, P. Zhao, X. Wang, Ferroelectric polarization-enhanced photoelectrochemical water splitting in TiO_2–$BaTiO_3$ core–shell nanowire photoanodes. *Nano Lett.* **15**, 7574–7580 (2015).
179. G. Liu, K. Du, J. Xu, G. Chen, M. Gu, C. Yang, K. Wang, H. Jakobsen, Plasmon-dominated photoelectrodes for solar water splitting. *J. Mater. Chem. A* **5**, 4233–4253 (2017).
180. H. Gao, C. Liu, H. E. Jeong, P. Yang, Plasmon-enhanced photocatalytic activity of iron oxide on gold nanopillars. *ACS Nano* **6**, 234–240 (2012).
181. S. Kim, Y. Yu, S. Y. Jeong, M. G. Lee, H. W. Jeong, Y. M. Kwon, J. M. Baik, H. Park, H. W. Jang, S. Lee, Plasmonic gold nanoparticle-decorated $BiVO_4$/ZnO nanowire heterostructure photoanodes for efficient water oxidation. *Catal. Sci. Technol.* **8**, 3759–3766 (2018).
182. Y. Duan, S. Zhou, Z. Chen, J. Luo, M. Zhang, F. Wang, T. Xu, C. Wang, Hierarchical TiO_2 nanowire/microflower photoanode modified with Au nanoparticles for efficient photoelectrochemical water splitting. *Catal. Sci. Technol.* **8**, 1395–1403 (2018).
183. F. Chen, W. Cui, J. Zhang, Y. Wang, J. Zhou, Y. Hu, Y. Li, S.-T. Lee, Photoelectroreduction of building-block chemicals. *Angew. Chem. Int. Ed.* **56**, 7181–7185 (2017).
184. R. Chen, K. Tian, D. He, T. Gao, G. Yang, J. Xu, H. Chen, D. Wang, Y. Zhang, Carboxylation of α,β-unsaturated ketones by CO_2 fixation through photoelectro-chemistry. *ACS Appl. Energy Mater.* **3**, 5813–5818 (2020).

185. C. Guo, P. He, R. Cui, Q. Shen, N. Yang, G. Zhao, Electrochemical CO_2 reduction using electrons generated from photoelectrocatalytic phenol oxidation. *Adv. Energy Mater.* **9**, 1900364 (2019).
186. F. Yarur Villanueva, J. Manioudakis, R. Naccache, M. B. Majewski, Carbon dot-sensitized photoanodes for visible light-driven organic transformations. *ACS Appl. Nano Mater.* **3**, 2756–2765 (2020).
187. S. Bhattacharjee, V. Andrei, C. Pornrungroj, M. Rahaman, C. M. Pichler, E. Reisner, Reforming of soluble biomass and plastic derived waste using a bias-free $Cu_{30}Pd_{70}$|perovskite|Pt photoelectrochemical device. *Adv. Funct. Mater.* **32**, 2109313 (2022).
188. B. Zhang, J. Jie, X. Zhang, X. Ou, X. Zhang, Large-scale fabrication of silicon nanowires for solar energy applications. *ACS Appl. Mater. Interfaces* **9**, 34527–34543 (2017).
189. X. Shen, M. Yao, K. Sun, T. Zhao, Y. He, C.-Y. Chi, C. Zhou, P. D. Dapkus, N. S. Lewis, S. Hu, Defect-tolerant TiO2-coated and discretized photoanodes for >600 h of stable photoelectrochemical water oxidation. *ACS Energy Lett.* **6**, 193–200 (2021).
190. Z. Wang, T. Hu, H. He, Y. Fu, X. Zhang, J. Sun, L. Xing, B. Liu, Y. Zhang, X. Xue, Enhanced H_2 production of TiO_2/ZnO nanowires co-using solar and mechanical energy through piezo-photocatalytic effect. *ACS Sustainable Chem. Eng.* **6**, 10162–10172 (2018).
191. K. P. Sokol, V. Andrei, Automated synthesis and characterization techniques for solar fuel production. *Nat. Rev. Mater.* **7**, 251–253 (2022).
192. Y. Teng, X.-D. Wang, J.-F. Liao, W.-G. Li, H.-Y. Chen, Y.-J. Dong, D.-B. Kuang, Atomically thin defect-rich Fe–Mn–O hybrid nanosheets as high efficient electrocatalyst for water oxidation. *Adv. Funct. Mater.* **28**, 1802463 (2018).
193. C. Liu, J. Qian, Y. Ye, H. Zhou, C.-J. Sun, C. Sheehan, Z. Zhang, G. Wan, Y.-S. Liu, J. Guo, S. Li, H. Shin, S. Hwang, T. B. Gunnoe, W. A. Goddard, S. Zhang, Oxygen evolution reaction over catalytic single-site Co in a well-defined brookite TiO_2 nanorod surface. *Nat. Catal.* **4**, 36–45 (2021).
194. Y. Yang, H. Yao, Z. Yu, S. M. Islam, H. He, M. Yuan, Y. Yue, K. Xu, W. Hao, G. Sun, H. Li, S. Ma, P. Zapol, M. G. Kanatzidis, Hierarchical nanoassembly of MoS_2/Co_9S_8/Ni_3S_2/Ni as a highly efficient electrocatalyst for overall water splitting in a wide pH range. *J. Am. Chem. Soc.* **141**, 10417–10430 (2019).
195. S. Chen, H. Huang, P. Jiang, K. Yang, J. Diao, S. Gong, S. Liu, M. Huang, H. Wang, Q. Chen, Mn-Doped RuO_2 nanocrystals as highly active electrocatalysts for enhanced oxygen evolution in acidic media. *ACS Catal.* **10**, 1152–1160 (2020).
196. R. D. L. Smith, B. Sporinova, R. D. Fagan, S. Trudel, C. P. Berlinguette, Facile photochemical preparation of amorphous iridium oxide films for water oxidation catalysis. *Chem. Mater.* **26**, 1654–1659 (2014).
197. Y. Chen, C. W. Li, M. W. Kanan, Aqueous CO_2 reduction at very low overpotential on oxide-derived Au nanoparticles. *J. Am. Chem. Soc.* **134**, 19969–19972 (2012).
198. J. Gu, C.-S. Hsu, L. Bai, H. M. Chen, X. Hu, Atomically dispersed Fe^{3+} sites catalyze efficient CO_2 electroreduction to CO. *Science* **364**, 1091–1094 (2019).
199. M. Liu, Y. Pang, B. Zhang, P. De Luna, O. Voznyy, J. Xu, X. Zheng, C. T. Dinh, F. Fan, C. Cao, F. P. G. de Arquer, T. S. Safaei, A. Mepham, A. Klinkova, E. Kumacheva, T. Filleter, D. Sinton, S. O. Kelley, E. H. Sargent, Enhanced electrocatalytic CO_2 reduction via field-induced reagent concentration. *Nature* **537**, 382–386 (2016).
200. D. Kim, S. Yu, F. Zheng, I. Roh, Y. Li, S. Louisia, Z. Qi, G. A. Somorjai, H. Frei, L.-W. Wang, P. Yang, Selective CO_2 electrocatalysis at the pseudocapacitive nanoparticle/ordered-ligand interlayer. *Nat. Energy* **5**, 1032–1042 (2020).
201. X. Chen, H. Chen, W. Zhou, Q. Zhang, Z. Yang, Z. Li, F. Yang, D. Wang, J. Ye, L. Liu, Boron dopant induced electron-rich bismuth for electrochemical CO_2 reduction with high solar energy conversion efficiency. *Small* **17**, 2101128 (2021).
202. T. Zheng, C. Liu, C. Guo, M. Zhang, X. Li, Q. Jiang, W. Xue, H. Li, A. Li, C.-W. Pao, J. Xiao, C. Xia, J. Zeng, Copper-catalysed exclusive CO_2 to pure formic acid conversion via single-atom alloying. *Nat. Nanotechnol.* **16**, 1386–1393 (2021).
203. J. Huang, X. Guo, G. Yue, Q. Hu, L. Wang, Boosting CH_3OH production in electrocatalytic CO_2 reduction over partially oxidized 5 nm cobalt nanoparticles dispersed on single-layer nitrogen-doped graphene. *ACS Appl. Mater. Interfaces* **10**, 44403–44414 (2018).
204. W. Zhang, Q. Qin, L. Dai, R. Qin, X. Zhao, X. Chen, D. Ou, J. Chen, T. T. Chuong, B. Wu, N. Zheng, Electrochemical reduction of carbon dioxide to methanol on hierarchical Pd/SnO_2 nanosheets with abundant Pd–O–Sn interfaces. *Angew. Chem. Int. Ed.* **57**, 9475–9479 (2018).
205. D. Raciti, K. J. Livi, C. Wang, Highly dense Cu nanowires for low-overpotential CO_2 reduction. *Nano Lett.* **15**, 6829–6835 (2015).
206. F. Hu, L. Yang, Y. Jiang, C. Duan, X. Wang, L. Zeng, X. Lv, D. Duan, Q. Liu, T. Kong, J. Jiang, R. Long, Y. Xiong, Ultrastable Cu catalyst for CO_2 electroreduction to multicarbon liquid fuels by tuning C–C coupling with CuTi subsurface. *Angew. Chem. Int. Ed.* **60**, 26122–26127 (2021).
207. J. Du, S. Li, S. Liu, Y. Xin, B. Chen, H. Liu, B. Han, Selective electrochemical reduction of carbon dioxide to ethanol via a relay catalytic platform. *Chem. Sci.* **11**, 5098–5104 (2020).
208. W. Liu, P. Zhai, A. Li, B. Wei, K. Si, Y. Wei, X. Wang, G. Zhu, Q. Chen, X. Gu, R. Zhang, W. Zhou, Y. Gong, Electrochemical CO_2 reduction to ethylene by ultrathin CuO nanoplate arrays. *Nat. Commun.* **13**, 1877 (2022).
209. H. Mistry, A. S. Varela, C. S. Bonifacio, I. Zegkinoglou, I. Sinev, Y.-W. Choi, K. Kisslinger, E. A. Stach, J. C. Yang, P. Strasser, B. R. Cuenya, Highly selective plasma-activated copper catalysts for carbon dioxide reduction to ethylene. *Nat. Commun.* **7**, 12123 (2016).
210. D. Kim, C. S. Kley, Y. Li, P. Yang, Copper nanoparticle ensembles for selective electroreduction of CO_2 to C_2–C_3 products. *Proc. Natl. Acad. Sci. U. S. A.* **114**, 10560–10565 (2017).
211. J. Qiu, G. Zeng, M.-A. Ha, M. Ge, Y. Lin, M. Hettick, B. Hou, A. N. Alexandrova, A. Javey, S. B. Cronin, Artificial photosynthesis on TiO_2-passivated InP nanopillars. *Nano Lett.* **15**, 6177–6181 (2015).
212. B. Zhou, X. Kong, S. Vanka, S. Cheng, N. Pant, S. Chu, P. Ghamari, Y. Wang, G. Botton, H. Cuo, Z. Mi, A GaN:Sn nanoarchitecture integrated on a silicon platform for converting CO_2 to HCOOH by photoelectrocatalysis. *Energy Environ. Sci.* **12**, 2842–2848 (2019).

Acknowledgments

Funding: V.A. is grateful for support from the Winton Programme for the Physics of Sustainability and the Kavli Energy NanoScience Institute (Winton—Kavli ENSI Exchange Fellowship). This work was supported by Liquid Sunlight Alliance, which is supported by the U.S. Department of Energy, Office of Science, Office of Basic Energy Sciences, Fuels from Sunlight Hub, under award DE-SC0021266. **Author contributions:** V.A. and I.R. drafted the manuscript and the original figures. V.A., I.R., and P.Y. conceived, discussed, and revised the manuscript. P.Y. supervised the work. **Competing interests:** The authors declare that they have no competing interests. **Data and materials availability:** All data needed to evaluate the conclusions in the paper are present in the paper.

Submitted 15 September 2022
Accepted 5 January 2023
Published 10 February 2023
10.1126/sciadv.ade9044